Three-Dimensional Steerable Magnetic Field (3DSMF) Sensor System for Classification of Buried Metal Targets

SERDP Project MM-1314
Final Technical Report

NSTD-05-693
July 2006

Carl V. Nelson
Deborah P. Mendat
Toan B. Huynh
Liane C. Ramac-Thomas
James D. Beaty
Joseph N. Craig

JOHNS HOPKINS
UNIVERSITY

Applied Physics Laboratory
11100 Johns Hopkins Road
Laurel MD 20723-6099
240-228-5000 / Washington
443-778-5000 / Baltimore

Distribution Statement A: Approved for Public Release, Distribution is Unlimited

This report was prepared under contract to the Department of Defense Strategic Environmental Research and Development Program (SERDP). The publication of this report does not indicate endorsement by the Department of Defense, nor should the contents be construed as reflecting the official policy or position of the Department of Defense. Reference herein to any specific commercial product, process, or service by trade name, trademark, manufacturer, or otherwise, does not necessarily constitute or imply its endorsement, recommendation, or favoring by the Department of Defense.

TABLE OF CONTENTS

Table of Contents ii

List of Figures iv

List of Tables vii

Abbreviations and Acronyms viii

1 Executive Summary 1

2 Introduction 2

2.1 Background 2
2.2 Project Objectives 3
2.3 Technical Approach 4

3 Rationale for 3DSMF 5

3.1 Conventional EMI Sensor 5
3.2 Single-Axis Horizontal Magnetic Field Antenna 7
3.2.1 Target and Field Uniformity 10
3.2.2 Field Strength Versus Distance 11

4 Target Identification with 3DSMF 13

4.1 Basic Formalism 13
4.2 Examples 14

5 3DSMF Modeling and Design 18

5.1 3DSMF Basic Design Concept 18
5.2 Design Modeling 19
5.2.1 Transmitter Modeling 19
5.2.2 Receiver Modeling 24

6 Fabrication and Initial Testing 28

6.1 Sensor System Fabrication 28
6.2 Transmitter Control Development 30
6.3 Receiver Optimization 34
6.3.1 Initial Configuration 34
6.3.2 Switched-Coil Receivers 35
6.3.3 Three-axis Receivers 38
6.3.4 Differential Configuration 39
6.3.5 Residual Compensation 40
6.4 Data Acquisition System (DAS) Development 40
6.5 Initial Laboratory Testing 47

7 2005 Activity 48

7.1 Final 3DSMF Antenna Configuration 48
7.1.1 Transmitters 48

7.1.2 Receivers 49
7.2 Data Analysis 50
7.2.1 X-, Y-, & Z-Channel Response 51
7.2.2 Time Decay Constants 53
7.2.3 Target Orientation 57
7.2.3.1 Coil Analysis 58
7.2.3.2 Pipe Analysis 60

Acknowledgement 66

References 67

LIST OF FIGURES

Figure 1 3DSMF technical approach overview 4
Figure 2 Magnetic field lines around a loop antenna 7
Figure 3 HMF antenna geometry. 8
Figure 4 Magnetic field lines around a horizontal field antenna 8
Figure 5 Prototype HMF antenna 9
Figure 6 Calibration test of prototype HMF antenna 9
Figure 7 Experimental data for HMF antenna with complex steel target 9
Figure 8 Experimental data showing uniqueness of time decay for different metal targets 10
Figure 9 Magnetic field uniformity and target response. 11
Figure 10 HMF (B_x) and loop (B_z) antenna comparison 12
Figure 11 Transverse response 15
Figure 12. Z-response 15
Figure 13 Magnitude of total response 16
Figure 14 Transverse response of a horizontal object 17
Figure 15 Z-response of a horizontal object 17
Figure 16 Y-response of a horizontal object 17
Figure 17 Simplified concept of 3DSMF transmitters 18
Figure 18 3DSMF sensor system with concept of operation 19
Figure 19 Antenna model using Field Precision software 20
Figure 20 Magnetic field strength as a function of wire spacing for constant total current 21
Figure 21 Magnetic field strength as a function of distance to return current path 21
Figure 22 Magnetic field strength as a function of depth versus antenna width 22
Figure 23 X- and Y-MFVs at various depths for two Z-antenna element currents. 23
Figure 24 Magnetic field angle for HMF and dipole antennas 24
Figure 25 Antenna configuration that decouples transmitter and receiver signals 25
Figure 26 Top view of one proposed receiver loop arrangement. 25
Figure 27 Receiver response modeling software screen shot 26
Figure 28 Normalized receiver response for different A values. 26
Figure 29 Receiver response for different B values 26
Figure 30 Simplified block diagram of 3DSMF sensor system electronics 28
Figure 31 3DSMF antenna cart 29

Figure 32 3DSMF electronics cart 29
Figure 33 Target geometry 30
Figure 34 3DSMF 15º MFVs 30
Figure 35 Transmitter switch wiring 31
Figure 36 Measured magnetic fields 32
Figure 37 Transmitter startup switching overshoot 33
Figure 38 DC/DC converter power supplies 34
Figure 39 3DSMF linear power supplies 34
Figure 40 Magnetic field strengths versus control values 34
Figure 41 Two-element planar receiver 35
Figure 42 Receiver switch circuit 36
Figure 43 Receiver response, a) no switches and b) with switches 37
Figure 44 Small three-axis receiver 38
Figure 45 Three-axis 0.6m cube receiver 38
Figure 46 Illustration of system noise 39
Figure 47 Top view of secondary differential Z-receiver coils 40
Figure 48 Wireless Web-based data collection approach 41
Figure 49 Screen shots of ETD data collection and control computer interface 41
Figure 50 XSA-100 prototyping board 42
Figure 51 DCSS isolation board 43
Figure 52 Amplifier and ADC board 43
Figure 53 DAS PC/104 components 44
Figure 54 HP iPAQ h5550 Pocket PC 44
Figure 55 Noise level of DAS amplifier and ADC. 45
Figure 56 Sample data from receiver electronics 45
Figure 57 Interior picture of DAS and telemetry system hardware 46
Figure 58 Example of target signature banding due to timing jitter in DCSS. 46
Figure 59 3DSMF antenna in laboratory test position 47
Figure 60 Magnetic field magnitudes for varying X-Y-Z transmit control values 48
Figure 61 Final 3DSMF receiver configuration 49
Figure 62 Longitudinal and transverse responses 50
Figure 63 Geometry for φ responses 51

Figure 64 X-Y-Z receiver amplitude ratios for sphere 52
Figure 65 X-Y-Z time decay ratios for sphere 52
Figure 66 Exponential fit for coil data 54
Figure 67 Exponential fit for sphere data 54
Figure 68 Longitudinal exponential fit for pipe data 55
Figure 69 Transverse exponential fit for pipe data 55
Figure 70 Ratio of pipe transverse amplitude constants with depth 56
Figure 71 Ratio of pipe longitudinal amplitude constants with depth 57
Figure 72 Target geometry for analysis 57
Figure 73 Position: XYZ45, Measured Position: ,φ= 46, θ = 39 59
Figure 74 Position: YZ45, Measured Position: ,φ = 90, θ = 40 60
Figure 75 Position: XZ30, Measured Position: φ= 0, θ= 61 61
Figure 76 Position: Z0, Measured Position: φ= xx , θ = 0 62
Figure 77 Summary of pipe data for different depths 64

LIST OF TABLES

Table 1 3DSMF Data Acquisition Time 42
Table 2 Calculated Time Decays 56
Table 3 Actual vs. Measured Coil Position 59
Table 4 Actual vs. Measured Pipe Position for d = 12 inches 63
Table 5 Actual vs. Measured Pipe Position for d = 16 inches 63
Table 6 Actual vs. Measured Pipe Position for d = 20 inches 63
Table 7 Actual vs. Measured Pipe Position for Off Center Positions 64

ABBREVIATIONS AND ACRONYMS

3D	Three-dimensional
3DSMF	Three-Dimensional Steerable Magnetic Field
AC	Alternating Current
ADC	Analog-to-Digital Converter
ATR	Automatic Target Recognition
AWG	American Wire Gauge
BRAC	Base Realignment and Closure
DAS	Data Acquisition System
DCSS	Data Collection Sub-System
DoD	Department of Defense
DRAM	Dynamic Random Access Memory
emf	electromotive force
EMI	Electromagnetic Induction
ETD	Electromagnetic Target Discriminator
FAR	False Alarm Rate
FD	Frequency-Domain
FPGA	Field Programmable Gate Array
FTP	File Transfer Protocol
JHU/APL	The Johns Hopkins University Applied Physics Laboratory
MFV	Magnetic Field Vector
MOSFET	Metal Oxide Semiconductor Field Effect Transistor
MPT	Magnetic Polarizability Tensor
PC/104	Embedded computer system standard
Pd	Probability of Detection
PSD	Power Spectral Density
PVC	Polyvinyl Chloride
RAM	Random Access Memory
SERDP	Strategic Environmental Research and Development Program
SNR	Signal-to-Noise Ratio
TD	Time-Domain
TRC	Transmitter-to-Receiver Coupling
UXO	Unexploded Ordnance
WiFi	Wireless Fidelity 802.11 Network

1 EXECUTIVE SUMMARY

The Johns Hopkins University/Applied Physics Laboratory (JHU/APL) has developed a novel approach to metal target classification via an advanced Three-Dimensional Steerable Magnetic Field (3DSMF) Sensor System. The 3DSMF is a time-domain (TD) electromagnetic induction (EMI) sensor configured with a three-axis magnetic field generator and three receivers that measures the multiple components of buried unexploded ordnance (UXO) magnetic polarizability tensors (MPT).

The project began with sensor concept modeling and simulation, bread-boarding, testing of the system components, and development of the control software; all of which were completed in 2003. In 2004, the prototype antenna and control electronics were fabricated and integrated. A number of technical challenges were revealed during the integration test phase which resulted in hardware and software modifications to resolve the problems. Data analysis of laboratory testing with targets was conducted after configurations of the transmitters and receivers were finalized in 2005. This final report summarizes work completed throughout the project.

By late summer 2005, the 3DSMF Sensor System was fully functioning in the lab with three steerable magnetic field transmitters, a ten-turn loop Z-receiver antenna, and ten-turn quadrapole X- and Y-receiver antennas. We collected high quality laboratory data with calibration objects (wire loops, spheres, rings, and plates) as well as from some axially symmetric targets (pipes). Direct measurement of the magnetic fields plus data analysis from receiver measurements of simple two-dimensional targets confirmed the validity of the 3DSMF concept. At this point, we obtained Strategic Environmental Research and Development Program (SERDP) concurrence to collect additional laboratory data for algorithm development efforts instead of undergoing field testing due to our concerns about the “non-robust” nature of the prototype design.

The results from the current year show promise of confirming the 3DSMF identification concept when using libraries of target time decay constants. The spatial orientation of targets was determined at different depths using library constants which had been derived from calibration measurements made with that target at a single depth. There is also evidence that the orientation of a target can be determined even if the target is off-center of the antenna. Further data collection and analysis would characterize the effectiveness of the 3DSMF Sensor System in discriminating between different targets.

2 INTRODUCTION

2.1 BACKGROUND

The Department of Defense (DoD) Base Realignment and Closure (BRAC) process requires environmental restoration and mitigation of millions of acres of former military bases to render them safe before they are returned to public use. Remediation of land contaminated with unexploded ordnance (UXO) entails the detection of buried metallic anomalies. A commonly used sensor for UXO detection is the EMI metal detector. Conventional EMI metal detectors, using either frequency-domain (FD) or time-domain (TD) eddy current methods, can detect large metal targets such as metal-cased high-metal content mines and UXOs at both shallow and deep depths under a wide range of environmental and soil conditions. However, other metal objects (clutter) commonly found in the environment pose a major problem. Clutter comprises a large fraction of detected anomalies and represents a major cost contribution to UXO clean-up efforts because, in the absence of anomaly classification as UXO or as clutter object, the anomaly must be remediated or dug up. Time-efficient and cost-effective remediation will be realized only when the detected metal targets can be accurately classified, preferably in real- or near real-time.

Most EMI sensors do not take advantage of all the available information that is inherent in the metal target response. The sensors tend to measure only a single dimension of a target response or, in the case of a spatially scanned target, try to infer a multi dimensional response. Experimental EMI sensors that do attempt to generate a 3D magnetic field and measure a 3D target response do so with magnetic field antennas that have fixed and complex spatial magnetic field distributions [1].

With a conventional pulsed EMI metal detector, a current loop transmitter is placed in the vicinity of the buried metal target, and steady current flows in the transmitter for a sufficiently long time to allow the turn-on transients in the soil to dissipate. The transmitter loop current is then turned off. According to Faraday's Law, the collapsing magnetic field induces an electromotive force (emf) in nearby conductors, such as the metal target. This emf causes eddy currents to flow in the conductor. Because there is no energy to sustain the eddy currents, they begin to decrease with a characteristic decay time that depends on the size, shape, and electrical and magnetic properties of the conductor. The decay currents generate a secondary magnetic field that is detected by a magnetic field receiver located above the ground and coupled to the transmitter via a data acquisition and control system.

The direction of the magnetic field and the field strength generated by a conventional loop EMI metal detector are a complex function of the distance of the antenna to the target. As the antenna is moved over the target, data are collected from different antenna-target aspect angles. An automatic target recognition (ATR) algorithm attempts to combine the measured time or frequency signature from the target with the spatial data to perform target classification. Laboratory measurements of UXO signatures and ATR algorithm results show great potential for increased probability of detection (Pd) and low false alarm rate (FAR). However, moving sensor positional errors relative to the unknown UXO target location coupled with high noise levels and poor depth estimates result in poor ATR performance.

To improve ATR performance, JHU/APL developed a novel sensor concept called a Three-Dimensional Steerable Magnetic Field (3DSMF) Sensor System [2]. The sensor system is a TD-EMI sensor configured with a three-axis magnetic field generator. The 3DSMF transmitter excites metal objects with directionally varying magnetic field vectors (MFV) without the need to move the antenna spatially over the objects. A receiver system records the time-decay response of an object as a function of the excitation MFV. Algorithms will classify the objects based on the collected data. In addition, determination metal target orientation in the ground may be a by-product of the 3DSMF.

Compared to a conventional moving horizontal loop sensor system, the 3DSMF sensor system has several advantages that make the system attractive for improved target classification [3]:

- The MFV of the sensor is steered into the body coordinate system of the unknown metal object thus increasing the signal-to-noise ratio (SNR)
- The relative position of the sensor and target need not be known
- The target is illuminated with a relatively uniform magnetic field
- The magnetic field strength is relatively uniform with distance compared to a loop antenna
- The sensor directly measures the MPT of the target [4] without the need to infer it from spatial data
- Measurements are taken while the sensor is stationary over the target so that there are no motion induced errors

2.2 PROJECT OBJECTIVES

The project objectives were to develop the 3DSMF Sensor System and demonstrate that it directly measures the three components of the MPT of a metal object for target classification. The 3DSMF Sensor System employs wide bandwidth TD EMI sensor technology originally developed for a landmine detection project for the US Army [5, 6, 7, 8, 9] using custom designed and constructed electronics optimized for metal detection sensitivity and data collection speed.

The major technical objectives were:

- Model, design and fabricate a portable antenna that projects a magnetic field in all directions under computer control
- Develop a receiving sensor and portable data acquisition system (DAS) to measure the eddy current time decay response of a metal target
- Develop automatic target classification software based on collected target data
- Conduct validation experiments in laboratory and field trials

2.3 TECHNICAL APPROACH

Figure 1 shows the overview of the technical approach to develop the sensor system.

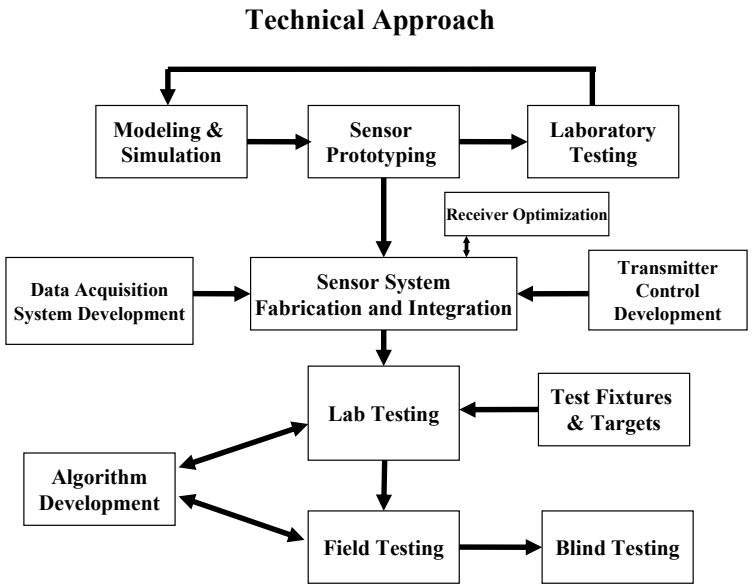

Figure 1 3DSMF technical approach overview

3 RATIONALE FOR 3DSMF

Extensive theoretical and experimental research supports the concept of metal target classification using EMI techniques. In the time-domain for a pulsed transmitter current, the eddy current time decay response from metal target can be expressed as:

$$V(t) = \delta(t) - \sum_i [A_i \exp\{-t/\tau_i\}] \qquad (1)$$

where **t** is time, **V(t)** is the induced voltage in the receiver coil, **δ(t)** is the delta function, $\mathbf{A_i}$ are object amplitude response coefficients, and $\boldsymbol{\tau_i}$ are the eddy current time decay constants of the object. Thus, the sensor response to a metal target is a sum of exponentials with a series of characteristic amplitudes, $\mathbf{A_i}$, and time constants, $\boldsymbol{\tau_i}$. Equation (1) and its complementary equation, i.e., in the frequency domain, form the theoretical basis of target classification using the EMI technique. If a metal target is shown to have a unique time decay response, a library of potential threat targets can be developed. When a metal target is encountered in the field, its time decay response can be compared to those in the library and, if a match is found, the metal target can be classified quickly. It is noted that Equation (1) is slightly different if the transmitter current waveform is a ramp or other time-varying signal, but the general nature of the multiple exponential target response is the same. Generally, for medium and large metal objects, the soil does not adversely affect the time decay response measurements because the soil response is small and/or confined to a small time decay region.

The magnetic field direction and the strength generated by a conventional EMI metal detector are a complex function of the distance between the antenna and its target. As the antenna is moved over the target, data are collected from different antenna-target aspect angles. An automatic target recognition (ATR) algorithm attempts to combine the measured time or frequency signature from the target with the spatial data to perform target classification. Although laboratory measurements of UXO signatures and ATR algorithm results show great potential for increased probability of detection (Pd) and low false alarm rate (FAR), laboratory successes are not mirrored in real-world field test results. Some potential reasons for the disparity are:

- ATR algorithms appear to need better SNR measurements of metal target signatures from both time or frequency domain sensor systems
- The motion of sensor platforms induce unacceptable levels of noise in the sensor data
- Moving sensor positional errors relative to the unknown UXO target location coupled with high noise levels and poor depth estimates result in poor ATR results

3.1 CONVENTIONAL EMI SENSOR

To appreciate the 3DSMF sensor and better understand its utility in target classification, we will briefly review a conventional horizontal loop and then describe the new sensor. As previously stated, most EMI metal detectors use a horizontal loop antenna to create a vertical magnetic field in the vicinity of a metal target for purposes of detection and classification. Typical loop antennas are formed from multiple turns of wire wound around a central axis. The magnetic

field direction and strength are a complex function of distance from the loop antenna. For example, the magnetic field on the axis of a circular loop varies as:

$$B \propto \frac{a^2}{\left[a^2 + z^2\right]^{3/2}} \qquad (2)$$

where **a** is the loop radius and **z** is the distance, on axis, from the plane of the loop. Far from the antenna, along the axis of the loop (greater than about two antenna diameters), the field strength varies approximately as $1/z^3$. Off-axis, the antenna field strength and direction tend to be a very complex function of position, with the field intensity particularly strong near the wires in the loop and weaker near the center of the loop. In cylindrical polar coordinates, the field for a circular loop is given by equation (3) [10]:

$$\begin{aligned} B_\rho &\propto \frac{z}{\rho\left[(a+\rho)^2 + z^2\right]^{1/2}}\left[-K + \frac{a^2+\rho^2+z^2}{(a-\rho)^2+z^2}E\right] \\ B_z &\propto \frac{1}{\left[(a+\rho)^2 + z^2\right]^{1/2}}\left[K + \frac{a^2-\rho^2-z^2}{(a-\rho)^2+z^2}E\right] \end{aligned} \qquad (3)$$

where **K** and **E** are complete elliptic functions of the first and second kind and $\boldsymbol{\rho}$ is the polar radial coordinate.

The above equations illustrate two major drawbacks to the magnetic field from a horizontal loop:

- complex spatial field strength
- relatively fast far-field strength fall-off with distance from the plane of the loop

Figure 2 illustrates the complicated nature of the magnetic field for a circular loop antenna. The complex spatial field excites the unknown buried metal target with a complex magnetic field. When a buried target of unknown depth and size is scanned with an EMI sensor, the spatial distribution of the excitation field at the target is largely unknown. If the field is complex at the target depth, the time or frequency response of the target to the field is not well characterized. This uncertainty may complicate or confound a target identification algorithm. The decay response measured by the EMI sensor receiver is a superposition of the many eddy current decay modes excited by the incident magnetic field. Separating the superimposed modes may make it difficult to classify the target.

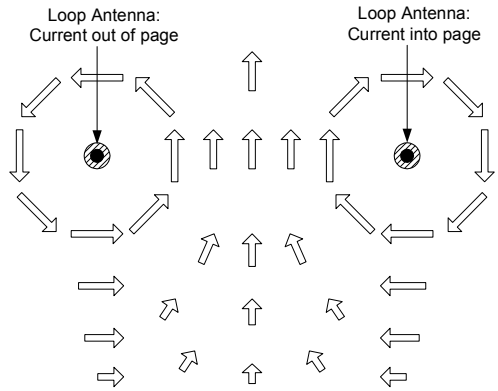

Figure 2 Magnetic field lines around a loop antenna

3.2 SINGLE-AXIS HORIZONTAL MAGNETIC FIELD ANTENNA

For an infinite conducting sheet current, the field in the direction parallel to the sheet current is given by:

$$B = \mu_0 \nu/2 \qquad (4)$$

where ν is the current density in the sheet. The magnetic field vector perpendicular to the sheet current is zero. Expressed another way, the sheet current is a horizontal magnetic field (HMF) generator or antenna. The important feature of (4) is the fact that the magnetic field is spatially constant.

We can approximate a sheet current using closely spaced, parallel current carrying wires. Using the Biot-Savart Law, we write the approximate X- and Z-components of the magnetic field:

$$B_x = \frac{\mu_0 I\, Z_0}{4\pi} \sum_{n=0}^{N} \left(\left[Z_0^{\,2} + (X_0 - n\Delta X)^2 \right]^{-1} \left[\frac{(L - Y_0)}{\sqrt{(L - Y_0)^2 + Z_0^{\,2} + (X_0 - n\Delta X)^2}} + \frac{Y_0}{\sqrt{Y_0^{\,2} + Z_0^{\,2} + (X_0 - n\Delta X)^2}} \right] \right)$$

$$B_z = \frac{\mu_0 I}{4\pi} \sum_{n=0}^{N} \left((X_0 - n\Delta X) \left[Z_0^{\,2} + (X_0 - n\Delta X)^2 \right]^{-1} \left[\frac{(L - Y_0)}{\sqrt{(L - Y_0)^2 + Z_0^{\,2} + (X_0 - n\Delta X)^2}} + \frac{Y_0}{\sqrt{Y_0^{\,2} + Z_0^{\,2} + (X_0 - n\Delta X)^2}} \right] \right) \qquad (5)$$

where N is the number of current elements (wires) carrying current I, Δx is the wire separation, L is the length of the antenna, and X_0, Y_0, and Z_0 are the location of the magnetic field measurement points in space. Equation (5) ignores the return path of the current. The current return path is important and when constructing the actual antenna, it was placed at a sufficiently large distance away from the nominal detection area as described later. Thus the true B_x component of the magnetic field will be slightly distorted from the values generated by the equation.

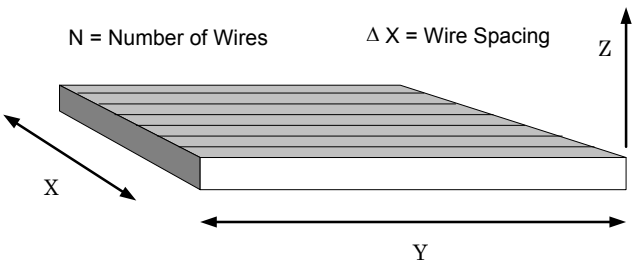

Figure 3 HMF antenna geometry.

Figure 4 shows the magnetic field lines for a set of closely spaced current carrying wires. Compared to Figure 2, the field lines of the HMF antenna are relatively uniform near the face of the plane containing the current carrying wires.

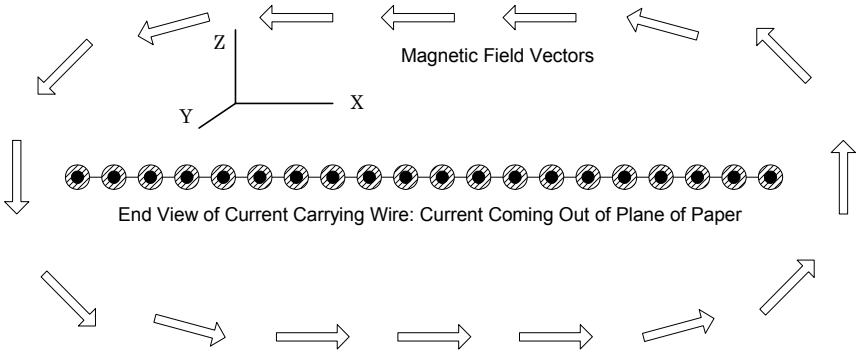

Figure 4 Magnetic field lines around a horizontal field antenna

JHU/APL constructed and built the prototype HMF antenna shown in Figure 5 for a US Army project. The data in Figure 6 shows that the field from this prototype HMF antenna is truly horizontal, and that data can be collected 10 μs after transmitter turn-off, demonstrating the high bandwidth of the sensor. Figure 7 is an example of experimental data collected with the HMF antenna for a complex steel target.

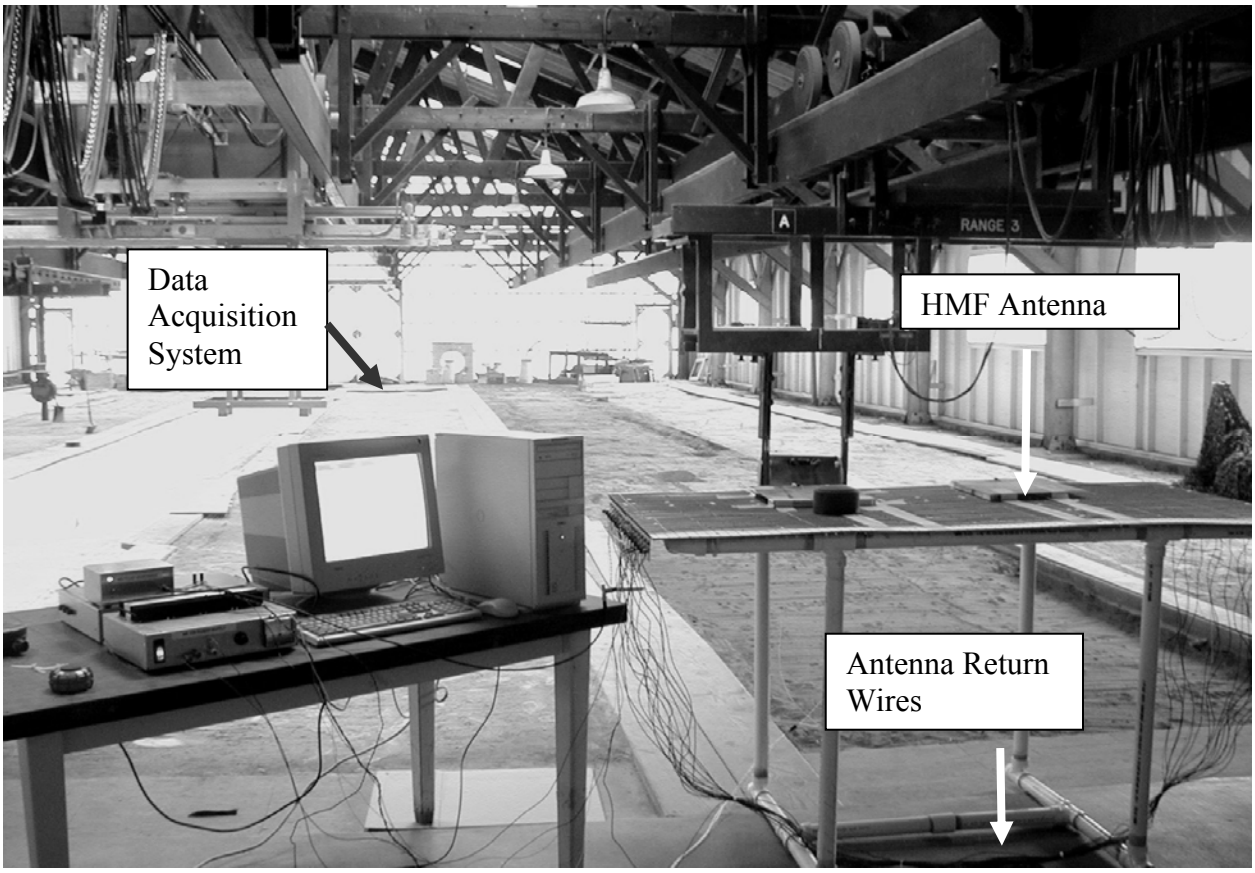

Figure 5 Prototype HMF antenna

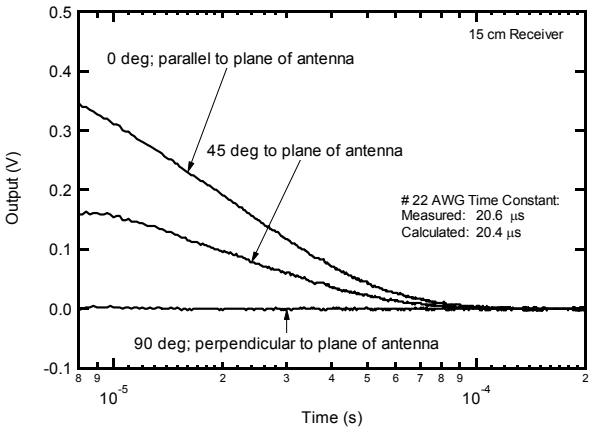

Figure 6 Calibration test of prototype HMF antenna

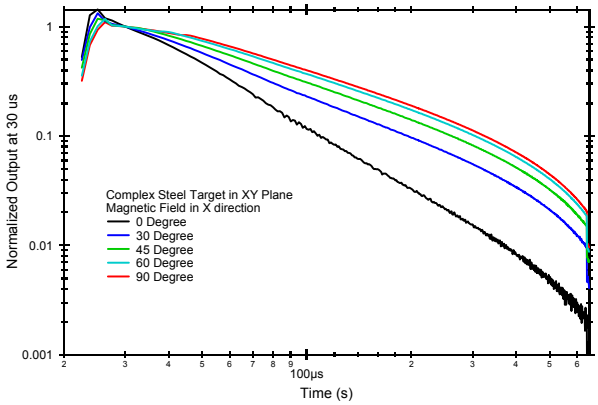

Figure 7 Experimental data for HMF antenna with complex steel target

The time decay response of the target depends on the orientation of the target relative to the antenna. The data in Figure 8 shows the uniqueness of horizontal and vertical time decays for different metal targets.

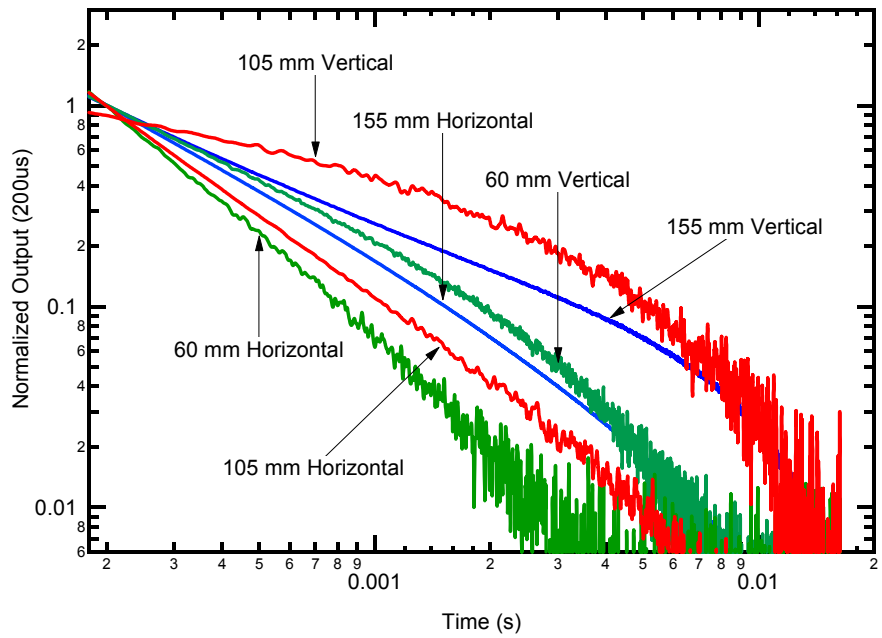

Figure 8 Experimental data showing uniqueness of time decay for different metal targets

3.2.1 TARGET AND FIELD UNIFORMITY

Why do we want to excite the unknown metal target with a uniform excitation magnetic field? For a simplified explanation to promote intuitive understanding, Figure 9 illustrates the basic physics of the problem. Consider a simplified extended target model made of two separated dipoles. Each dipole time decay constant is modeled as a single exponential decay and the sum of the two dipole time decays is the eddy current time decay signature of the target. In our example, dipole 1 has a decay time constant of $\boldsymbol{\tau_a}$ and an amplitude coefficient of $\mathbf{A_a}$, and dipole 2 has a decay time constant of $\boldsymbol{\tau_b}$ and an amplitude coefficient of $\mathbf{A_b}$. This signature is an inherent property of the target and is used for classification. Now consider the case, shown in Figure 9a, where we excite the target with a spatially varying (non-uniform) magnetic field that excites the two dipoles with different magnetic fields, B_1 and B_2. The target signature is now dependent on the excitation field and is not simply the sum of two exponential decays. This potentially makes target classification more difficult. In Figure 9b, the excitation magnetic field is uniform (B_u) over the target. In this case, the theoretical response of the target is preserved because the magnetic field can be factored out of the target response equation. We are left with only the target decay properties, independent of the details of the uniform excitation magnetic field.

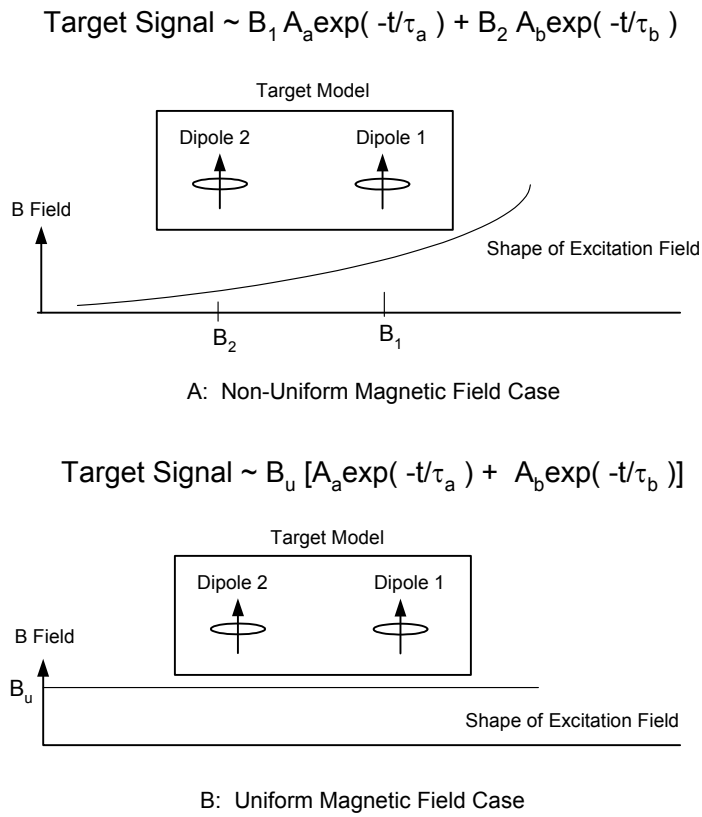

Figure 9 Magnetic field uniformity and target response.

3.2.2 FIELD STRENGTH VERSUS DISTANCE

In addition to improved horizontal spatial uniformity, the HMF antenna has more constant magnetic field intensity, compared to a conventional loop antenna, as a function of distance from the plane of the antenna. Figure 10 shows model results for a HMF antenna (1 m by 3 m) and a loop antenna (1 m diameter). The log-linear plot compares B_x and B_z versus distance from the plane of the antennas. The magnetic fields from each antenna have been normalized to one at a depth of 10 cm to show the relative field intensity fall-off with distance. The calculations were made at the center point of each antenna. Over the depth range of 10 cm to 5 m, the figure shows that the HMF antenna field strength, B_x, varies by approximately a factor of 30, while over the same depth range, the horizontal loop antenna field strength, B_z, varies by a factor of 1000. Also shown in the figure is a third curve of a HMF antenna with a return current path 1 m away from the primary antenna surface. The B_x field strength is lower than the HMF field without the return path, but the field still falls off more slowly than the loop antenna. Over the depth range of 10 cm to 500 cm, the HMF antenna field strength with a return path included varies by approximately a factor of 60; still much less than the loop antenna value of 1000.

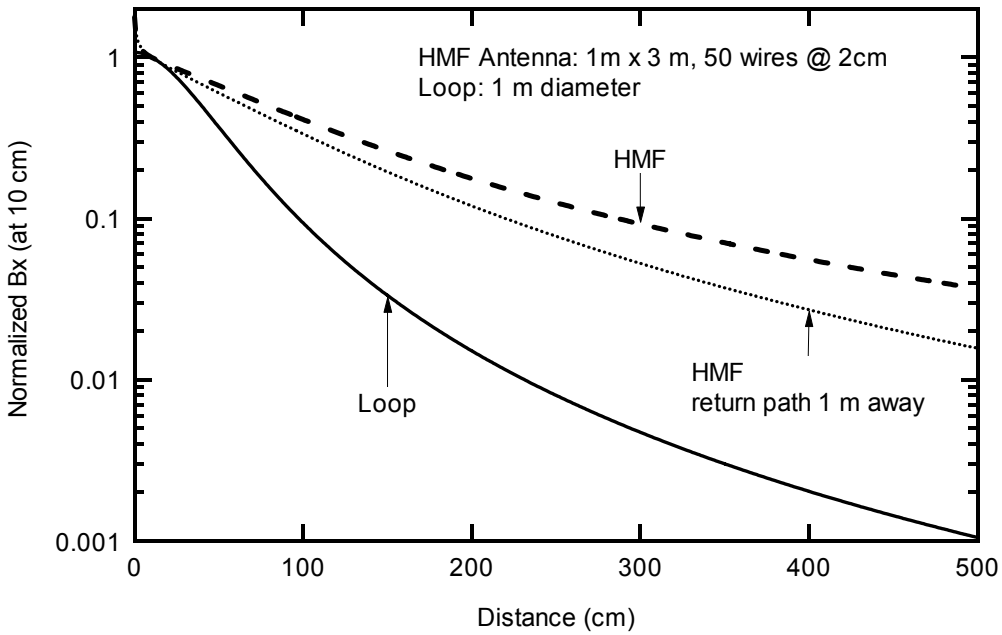

Figure 10 HMF (B_x) and loop (B_z) antenna comparison

4 TARGET IDENTIFICATION WITH 3DSMF

UXO objects have a unique eddy current time decay (or frequency) response characteristic so that they can be discriminated from a wide variety of typical metal clutter in a variety of soil types. UXO objects have many complex three-dimensional structural features that manifest themselves in different eddy current time decay or frequency spectrum characteristics. This complex eddy current decay response must be measured very accurately over many orders of magnitude in time and amplitude (TD sensor) or frequency, amplitude and phase (FD sensor).

For a TD EMI sensor, a metal target can be modeled by defining a magnetic polarizability tensor (MPT) that contains the primary magnetic response modes[2] of the target

$$B = \begin{bmatrix} \beta_x & 0 & 0 \\ 0 & \beta_y & 0 \\ 0 & 0 & \beta_z \end{bmatrix}, \qquad (6)$$

The diagonal components of the tensor are the time decay responses of the target to excitations in an orthogonal reference frame centered on the target. In an orthogonal XYZ coordinate system, β_x is the decay response to a magnetic field excitation in the X direction, β_y is the decay response to a magnetic field excitation in the Y direction, and $\beta_z(t)$ is the decay response to a magnetic field excitation in the Z direction. For an axially symmetric, or body of revolution, target, β_x and β_y are equal and the matrix can be written as:

$$B = \begin{bmatrix} \beta_t & 0 & 0 \\ 0 & \beta_t & 0 \\ 0 & 0 & \beta_l \end{bmatrix}, \qquad (7)$$

where β_l is longitudinal and β_t is transverse to the symmetry axis.

4.1 BASIC FORMALISM

The secondary magnetic field resulting from the induced dipole moment of such an object is:

$$\mathrm{m} = UBU^T \cdot \mathrm{H}. \qquad (8)$$

where H is the magnetic field at the object. The matrix U represents a transformation of coordinates from the internal body-centered coordinates of the object to the coordinate system in which the object resides and in which measurements are made.

If the measurement system includes a constant but steerable magnetic field, we can make this explicit and write:

$$\mathrm{m} = U_o B U_o^{\ T} \cdot U_s \mathrm{H}_a, \qquad (9)$$

where U_o represents the orientation of the object and U_s represents a rotation that steers the applied field to its desired orientation (for example, H_a might represent a constant magnetic field applied in the Z-direction and the combination $U_s H_a$ would represent the steered field.)

The rotation matrix is parameterized by a polar angle θ and an azimuth angle φ. It can be written as:

$$U(\varphi,\theta)=\begin{bmatrix}\cos\varphi & -\sin\varphi & 0\\ \sin\varphi & \cos\varphi & 0\\ 0 & 0 & 1\end{bmatrix}\begin{bmatrix}\cos\theta & 0 & \sin\theta\\ 0 & 1 & 0\\ -\sin\theta & 0 & \cos\theta\end{bmatrix}=\begin{bmatrix}\cos\varphi\cos\theta & -\sin\varphi & \cos\varphi\sin\theta\\ \sin\varphi\cos\theta & \cos\varphi & \sin\varphi\sin\theta\\ -\sin\theta & 0 & \cos\theta\end{bmatrix}. \quad (10)$$

Note that the rotation matrix is such that $U^{-1}= U^T$ so that $UU^T= U^TU = I$.

Putting in all of the angular dependencies, the induced magnetic field is

$$\mathrm{m} = U(\varphi_o,\theta_o)BU(\varphi_o,\theta_o)^T \cdot U(\varphi_s,\theta_s)\mathrm{H}_a . \quad (11)$$

Note the effect of the steering vector. If (φ_o, θ_o) is the same as (φ_s, θ_s) this means that the field is applied to the object as if the field is in the internal body-centered coordinates of the object. We have

$$U(\varphi_o,\theta_o)^T \cdot U(\varphi_s,\theta_s) = \mathrm{I}, \quad (12)$$

so that

$$\mathrm{m} = U(\varphi_o,\theta_o)B\mathrm{H}_a . \quad (13)$$

If the orientation of the object is known, the field can be steered in the body-centered coordinate system. Thus, the field can be steered to a direction that selectively excites either the longitudinal or transverse dipole moments or a specified combination of the two. In practice, the orientation, (φ_o,θ_o) of the object is unknown. However, it is possible to use measurements of m for multiple steering angles to deduce the orientation of the object and to identify its internal magnetic dipole moments.

4.2 EXAMPLES

The examples shown here are based on

$$B=\begin{bmatrix}1 & 0 & 0\\ 0 & 1 & 0\\ 0 & 0 & 4\end{bmatrix} \text{ and } \mathrm{H}=\begin{bmatrix}0\\ 0\\ 1\end{bmatrix}. \quad (14)$$

Vertical object:

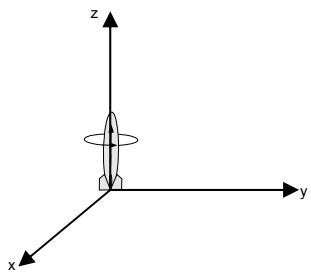

In this case the object is oriented such that only the longitudinal moment of the object is excited by an applied field in the Z-direction.

Figure 11 and Figure 12 depict the transverse and Z-responses when the applied field is steered in both azimuth and polar angle. As the response, m, is a vector, there are three components.

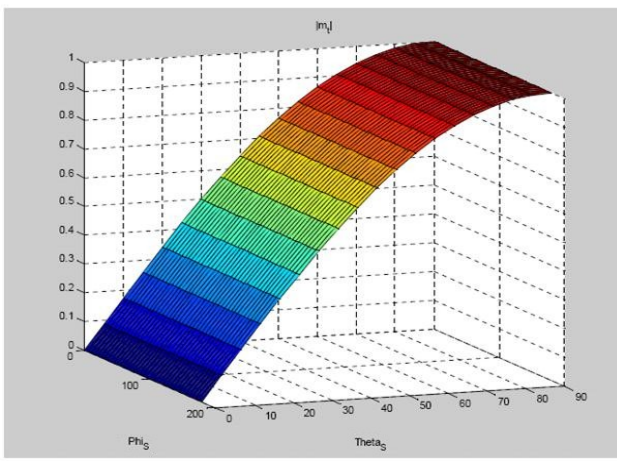

Figure 11 Transverse response

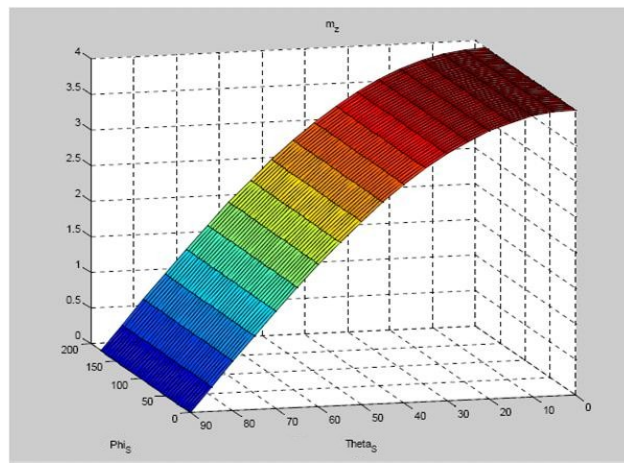

Figure 12. Z-response

The graphs of the X- and Y-components of the response would show what appear to be complicated patterns, whereas the Z-component of the response depends only on the polar angle, θ_s. If the X- and Y-components are combined to form the transverse component, the picture becomes simpler, and this is shown in Figure 11. The magnitude of the transverse response reaches a maximum value of 1 when $\theta_s = 90^\circ$ or when the applied field is transverse to the object. The response does not depend on φ_s because of the axial symmetry. The maximum value of the response is equal to the transverse moment of the object, and depends only on the transverse moment.

The longitudinal response (the Z-component) reaches its maximum value of 4 (equal to the value of the longitudinal moment) when the applied field is in the Z-direction ($\theta_s = 0^\circ$). Also in this case, the response does not depend on φ_s.

The magnitude of the total response ($|m|$) depends only on θ_s as shown in Figure 13.

The response of the vertical object to the applied field can be decomposed into longitudinal and transverse responses. Each of these responses is independent, and each depends only on the

corresponding magnetic dipole moment of the object. By steering the applied field appropriately, the two dipole moments can be excited independently.

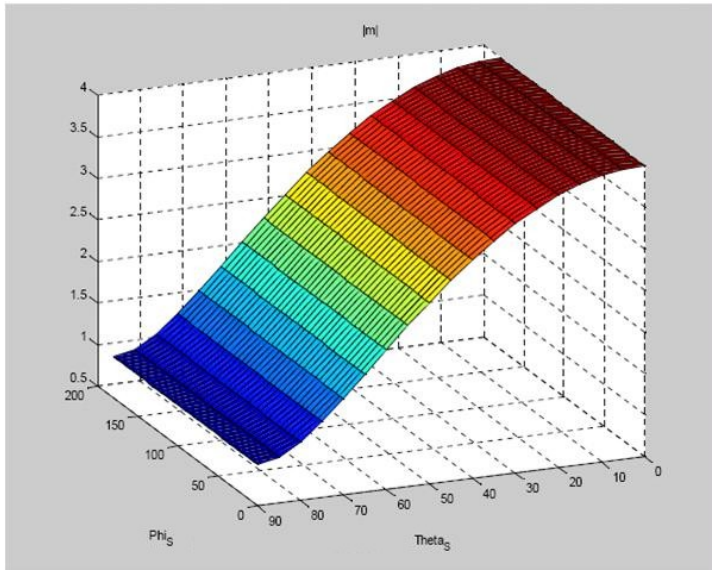

Figure 13 Magnitude of total response

Horizontal object:

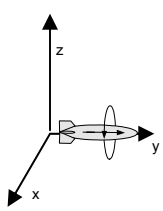

In this case, $\varphi_o = 90^\circ$ and $\theta_o = 90^\circ$. This situation is exactly the same as the previous example except that the object has been rotated so that the y-axis now takes the place of the previous Z-axis and the transverse response lies in the Z-X plane.

It is instructive to look at the response in the Z-X plane as shown in Figure 14. The response depends only on the transverse magnetic dipole moment. The maximum response is reached when $\varphi_s = 0^\circ$. When $\varphi_s = 90^\circ$ and $\theta_s = 90^\circ$, the transverse response goes to zero as the magnetic field is aligned with the longitudinal axis of the object.

The Z-component of the response also depends only on the transverse magnetic dipole moment. This is because the longitudinal magnetic dipole moment is parallel to the Y-axis and produces a response only in the Y-direction. This is shown in Figure 15. The response in the Y-direction, shown in Figure 16, is due to the longitudinal magnetic moment and reaches its maximum value when $\varphi_s = 90^\circ$ and $\theta_s = 90^\circ$.

This example demonstrates that it is necessary to measure more than the Z-component of the magnetic response if one hopes to measure quantities related to the longitudinal magnetic dipole moment for horizontal objects.

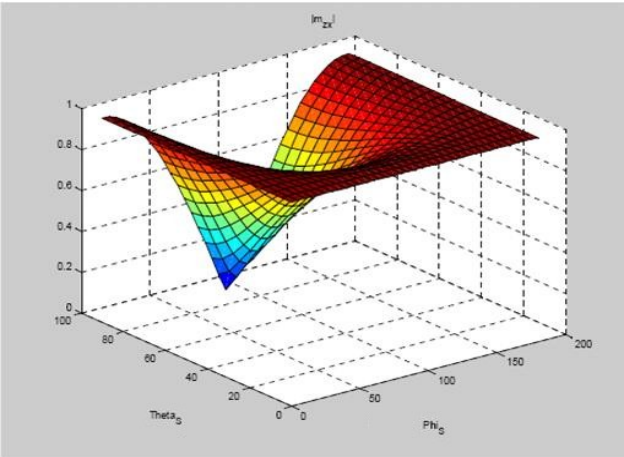

Figure 14 Transverse response of a horizontal object

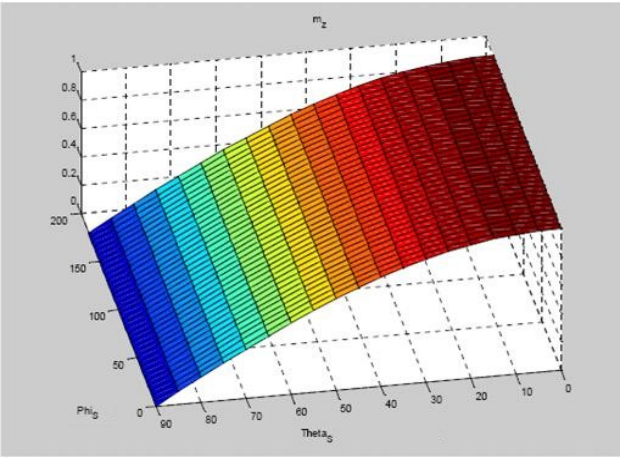

Figure 15 Z-response of a horizontal object

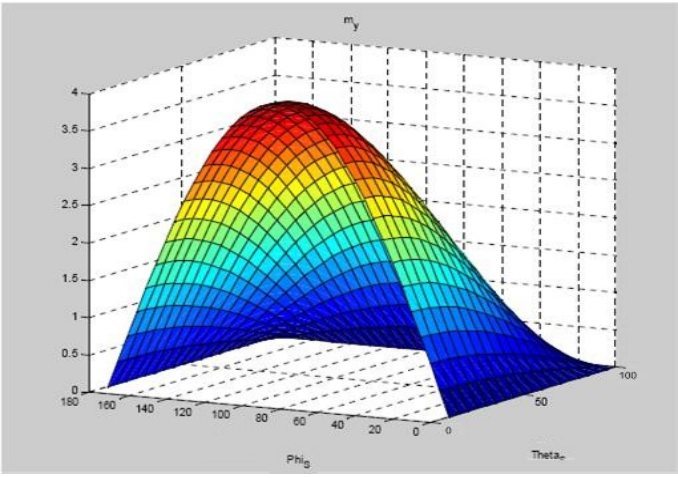

Figure 16 Y-response of a horizontal object

5 3DSMF MODELING AND DESIGN

5.1 3DSMF BASIC DESIGN CONCEPT

Previous experimental results from the prototype HMF antenna system [5] validated the HMF concept. The next step was to take advantage of the HMF antenna properties and make a 3DSMF sensor. To conceptualize the 3DSMF sensor system, we considered two single-axis HMF antennas co-located at right angles to each other. This arrangement forms a two-dimensional horizontal field-generating antenna. The third dimension to the magnetic field is created by adding a horizontal loop antenna to the two HMF antennas as shown in Figure 17. Thus, we create a magnetic field vector in three-dimensional space by varying the current in each antenna element employing superposition of the fields of each antenna. One way to look at the 3DSMF sensor is this: instead of measuring the response of the target to a fixed orthogonal magnetic field from a conventional 3D magnetic field sensor, the 3DSMF sensor rotates the magnetic field coordinate system into the target body coordinate system, thus simplifying the classification process. In addition, the process of orienting the excitation field into the target body coordinate system potentially gives an indication of the target orientation in the ground.

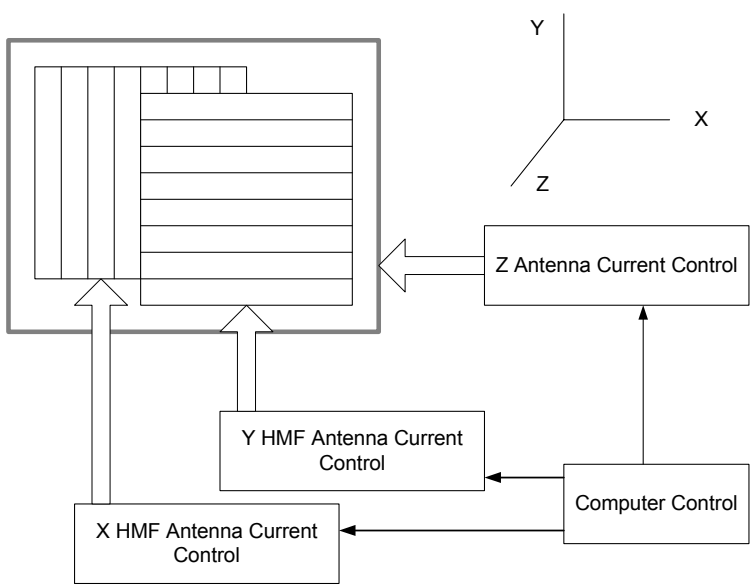

Figure 17 Simplified concept of 3DSMF transmitters

Figure 18 shows a 3D cartoon of the antenna operation. The sensor generates MFV that are sequentially rotated through 3D space. Target time decay responses are measured at each MFV position. The target decay responses measured at each MFV position are then used in an algorithm for target classification.

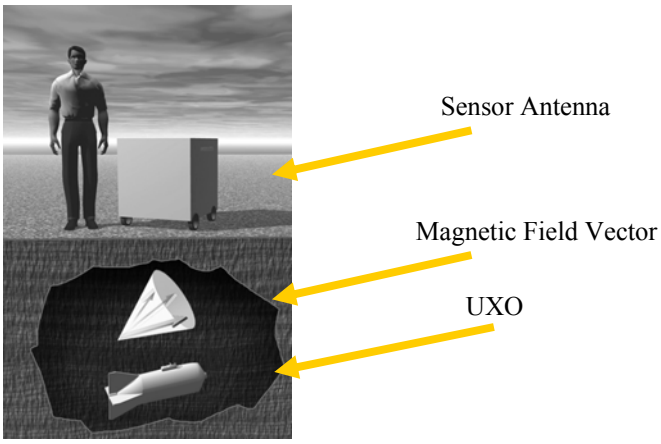

Figure 18 3DSMF sensor system with concept of operation

5.2 DESIGN MODELING

5.2.1 TRANSMITTER MODELING

A primary activity during the system design phase was to develop an EMI sensor with a steerable magnetic field and a field strength that is relatively uniform in volume below the antenna. Defining uniformity and establishing the size of the sensing volume were two of the modeling effort objectives. It appears that we can define a volume, centered on the antenna, of about 40 cm horizontally and 60 cm in depth where we have an MFV variation of about 15º. In contrast, a dipole antenna has an MFV variation of about 35º over the same volume. Using the cosine rule for excitation response, we found the HMF antenna error is (1-cos(15º)) ≈ 3% and the dipole antenna error is (1-cos(35º)) ≈ 18%. For a 2 m square antenna in the region ± 20 cm relative to the center of the antenna, the horizontal magnetic field variation is on the order of ± 10 %. Over the depth range of ± 20 cm, centered at 40 cm depth, the vertical magnetic field variation is about 20%. The 60 cm depth is not a limiting factor for the sensor system to acquire target signatures; the sensor should be able to measure signatures much deeper.

Using magnetic field modeling software from Field Precision, we performed parametric analyses of the magnetic fields for a 3DSMF transmitter. Figure 19 shows a screen shot from the Field Precision magnetic field modeling software for the antenna. The objective was to establish antenna parameters that created a relatively uniform and electronically 3D steerable magnetic field in a useful volume below the antenna.

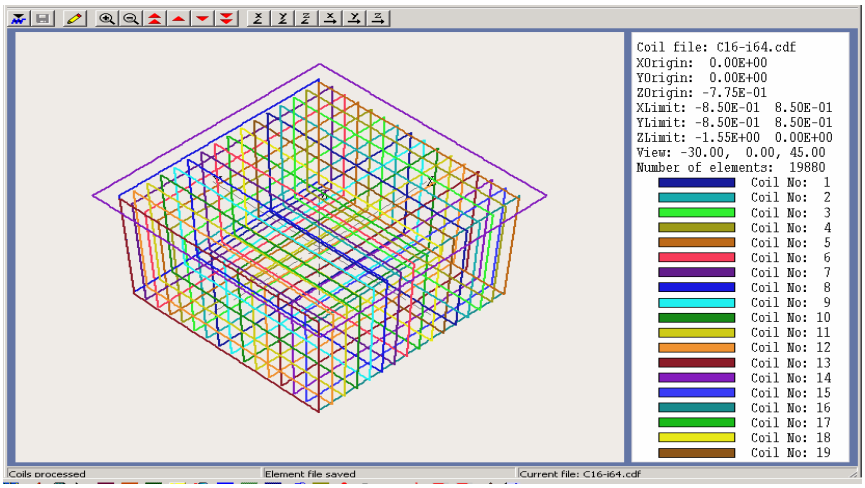

Figure 19 Antenna model using Field Precision software

The antenna parameters to be optimized were:

- Wire spacing versus field strength
- Return current path separation distance
- Width versus field strength and uniformity
- Magnetic field steering versus field uniformity

The first analysis sought to characterize the uniformity and field strength of the magnetic field against the practical constraint of wire spacing for a given antenna size. The field uniformity under investigation was the local field variation caused by the individual wires. The bandwidth of the sensor is dependent on the turn-off time of the transmit antenna, so for optimum performance each wire requires its own electronic switch. For a given antenna width, the number of wires/switches is directly related to the wire spacing. Also, as the number of wires increase, for a fixed wire size the power dissipation increases. Increasing the wire size to compensate for increased wire resistance increases the weight and cost of the antenna. Therefore, we wished to minimize the number of wires while still generating a strong magnetic field with good uniformity.

In the absence of an absolute design requirement, we selected 10% local magnetic field uniformity at 20 cm depth as a goal for the HMF. We then modeled different wire spacing for a fixed 1.5 m wide antenna. The results of the modeling indicated that wires spaced about 8 to 10 cm apart gave relatively good results.

We also studied the wire spacing from the point of view of total power consumption. Figure 20 shows magnetic field strength at the center of the antenna for wire spacing from 2.4 to 50 cm, with the total power dissipated by the antenna kept constant. The data shows that, under this power constraint, there are small gains in field strength with wire spacing closer than about 5-10 cm. However, from Equation (5), the magnetic field strength is directly proportional to the wire

spacing (e.g., current density). Because it is easier to remove wires from the hardware than to add them later, the initial prototype design was constructed with 2.5 cm wire spacing to allow future flexibility.

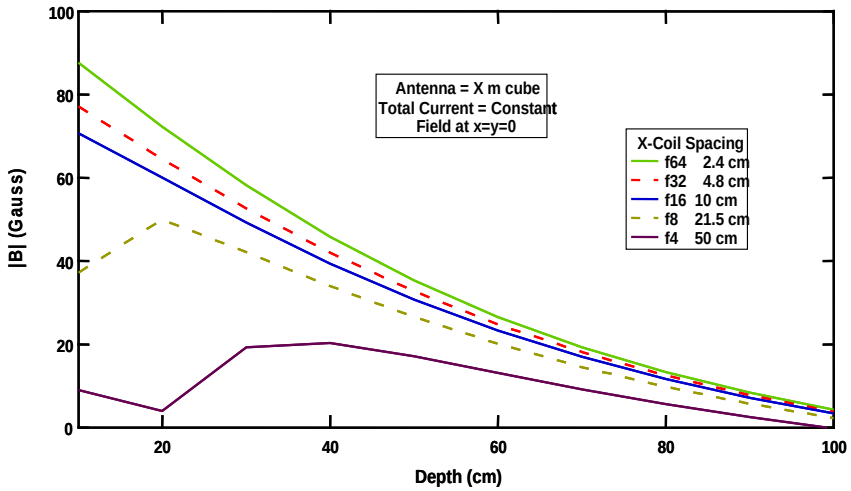

Figure 20 Magnetic field strength as a function of wire spacing for constant total current

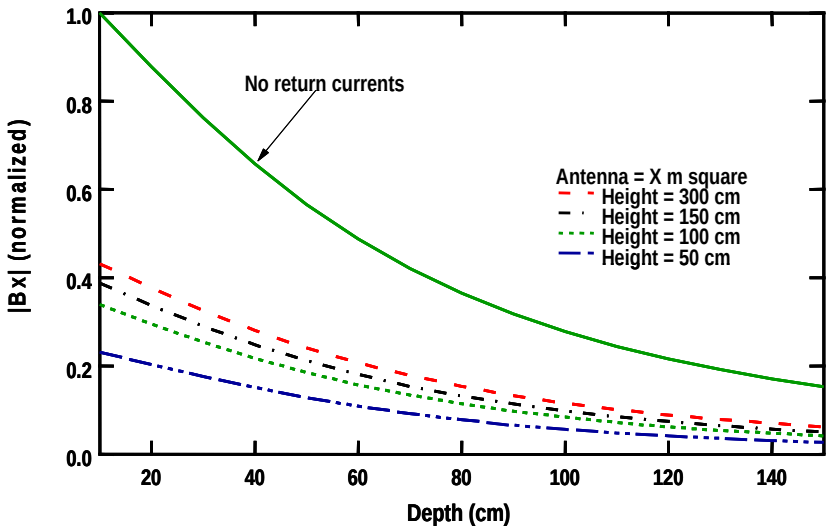

Figure 21 Magnetic field strength as a function of distance to return current path

A practical HMF field generator was constructed by winding the antenna wires around a box form. The target excitation component of the magnetic field is generated by the plane of wires closest to the ground. However, this primary field is reduced by the superposition of the magnetic field in the opposite direction generated by the return current path from the top of the box. For the return current path separation distance study, we took a 1.5 m by 1.5 m square antenna as an initial antenna size. We then varied the separation distance of the return current path and studied the magnetic field fall-off at the center of the antenna versus depth. A summary of the results is shown in Figure 21. The plots show the field fall-off for "no return path," which represents the idealized antenna, and for 3 m, 1.5 m, 1.0 m and 0.5 m return path separation. A 3

m separation distance was deemed impractical due to the sheer size of the resulting mechanical structure. There is an improvement of only about 15 % in field strength between the 1 m and 1.5 m antennas. The initial sensor design used an antenna separation distance of 1 m. The small signal strength penalty of 15 % appeared to be a reasonable price to pay for an antenna that would be smaller, lighter in weight, easier to handle in the field and consume less power due to wire resistance than an antenna with 1.5 m separation distance.

Figure 22 shows results of antenna width modeling. With a fixed return path of 1 m, the width of the antenna (assuming a square HMF generator) was varied and the field strength was plotted as a function of depth. As expected, the wider antenna had the least field strength fall-off with distance. Of the four antennas studied, the 3 m wide antenna had the lowest fall-off rate followed by the 2 m antenna. While a zero fall-off rate for the magnetic field would be ideal, it would necessitate an infinite width.

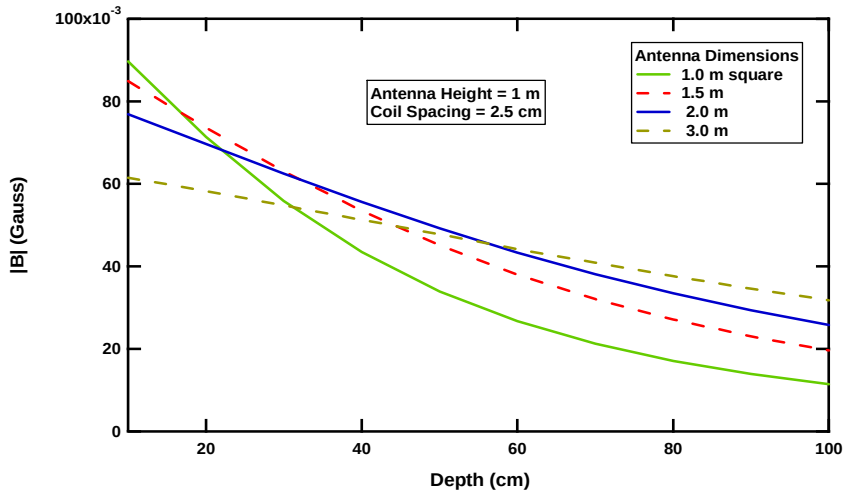

Figure 22 Magnetic field strength as a function of depth versus antenna width

In the absence of a specific design requirement for depth uniformity, the 2m antenna width was selected for the prototype construction. This was the largest practical size antenna in terms of weight and mechanical structure that could be shipped and deployed under field conditions when constructed using low-cost plastic pipe. With a return path of 1 meter, the antenna is about 1 m by 2 m by 2 m in size. The antenna was mounted on wheels to facilitate field operations.

In addition to their dramatically different spatial properties, HMF and loop antennas in this size range have different magnetic field strengths; therefore, a combined HMF and loop antenna was modeled to investigate electronic steering of the 3DSMF sensor. Steering the antenna in horizontal directions is achieved by varying the currents in the X- and Y-elements of the antenna array. Equal current in each element yields a 45º MFV in the horizontal plane. Steering the antenna out of the XY plane is achieved by varying the current in the Z-element. Because the maximum current in each of the X- and Y-elements is dictated by both the desired detection depth and by practical transmitter design constraints, it was necessary to determine that sufficient vertical steering was achievable. The plots in Figure 23 show both the variation in MFV and uniformity of the MFV with depth for a 2 m x 2 m HMF antenna and a co-located 2 m horizontal

loop (Z-direction) antenna. The MFV variation is caused by the field lines curving around the antenna as depicted previously in Figure 4 and is a function of the width of the antenna. The family of curves in the graphs depicts the MFV across the X- or Y-axis at depths from 10 to 100 cm. The left plot represents no vertical field (i.e., Z-element current equal to zero) and shows an MFV at the origin of 0º. On the right, the plot shows that, with an easily realizable current in the Z-element loop antenna, the MFV changes to approximately 45º. If we can generate a 45º angle in each of the three directions, then by symmetry, we can cover the entire 3D space. Both plots demonstrate that the MFV has good linearity (± 15º) in the target region of ± 20 cm horizontally and 10 to 100 cm in depth. The results of this analysis demonstrate that 3D steering is possible in a realizable 3DSMF design.

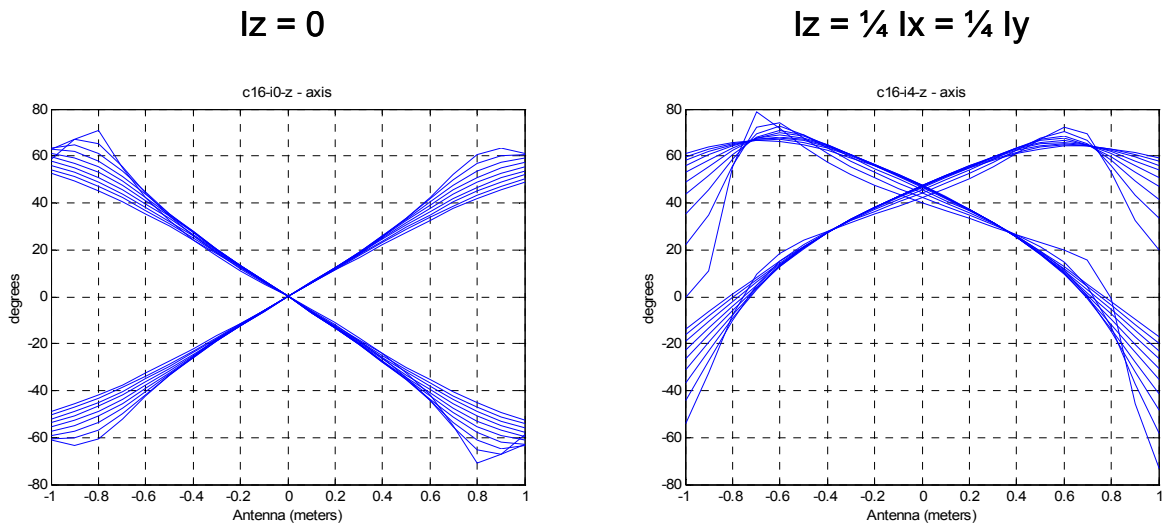

Figure 23 X- and Y-MFVs at various depths for two Z-antenna element currents.

As discussed in Section 3.1, variation in the MFV should be minimized over the length of the target for accurate target classification. To appreciate the MFV spatial uniformity of a HMF antenna, Figure 24 compares the MFV of a 1.5 m diameter dipole antenna turned on its side (to create a horizontal magnetic field) with a 1.5 m by 1.5 m HMF antenna. The data are modeled at 30 cm depth. The HMF antenna has a maximum angular deviation of about 15º, 20 cm from the center of the HMF antenna, while the dipole antenna has a maximum angular deviation of about 35º, 20 cm from the center of the dipole antenna.

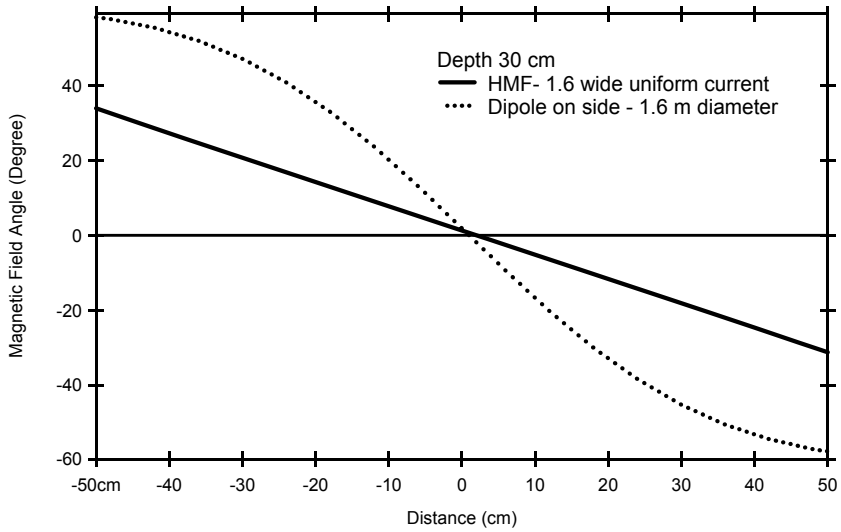

Figure 24 Magnetic field angle for HMF and dipole antennas

5.2.2 RECEIVER MODELING

Figure 25 is a simplified block diagram for one potential receiver system approach. The HMF antenna is centered over a target and excites the target with a horizontal magnetic field. Induction loop magnetic field receivers are located symmetrically about the centerline of the antenna plane. Figure 26 shows a top view of the quadrature receiver loop arrangement. The receiver loops are wound in the same direction and connected to a differential amplifier. The flux from the target through the right receiver is in the positive Z direction and flux through the left receiver is in the negative Z direction. The output of the differential amplifier can be written as:

$$V = (T1 + N1 + A1) - ((-T2) + N2 + A2) \qquad (15)$$

where V is the output voltage of the amplifier, T1 is target signal output from the right receiver loop (positive flux), N1 is noise seen by the right receiver loop, A1 is magnetic field flux coupling from the vertical magnetic field antenna into the right receiver, T2 is the output from the left receiver loop (negative flux), A2 is magnetic field flux coupling from the vertical magnetic field antenna into the left receiver, and N2 is noise seen by the left receiver. In this analysis we have ignored the flux coupling from the HMF antennas because the field is small parallel to the plane of the HMF antenna. To first order approximation, the far-field noises N1 and N2 are equal, and the antenna couplings A1 and A2 are equal. From Equation (15), the output from the amplifier reduces to $V \approx T1 + T2$. This particular receiver arrangement reduces far-field noise (e.g., power line, AM radio stations, and electronic equipment noise) and vertical magnetic field antenna coupling.

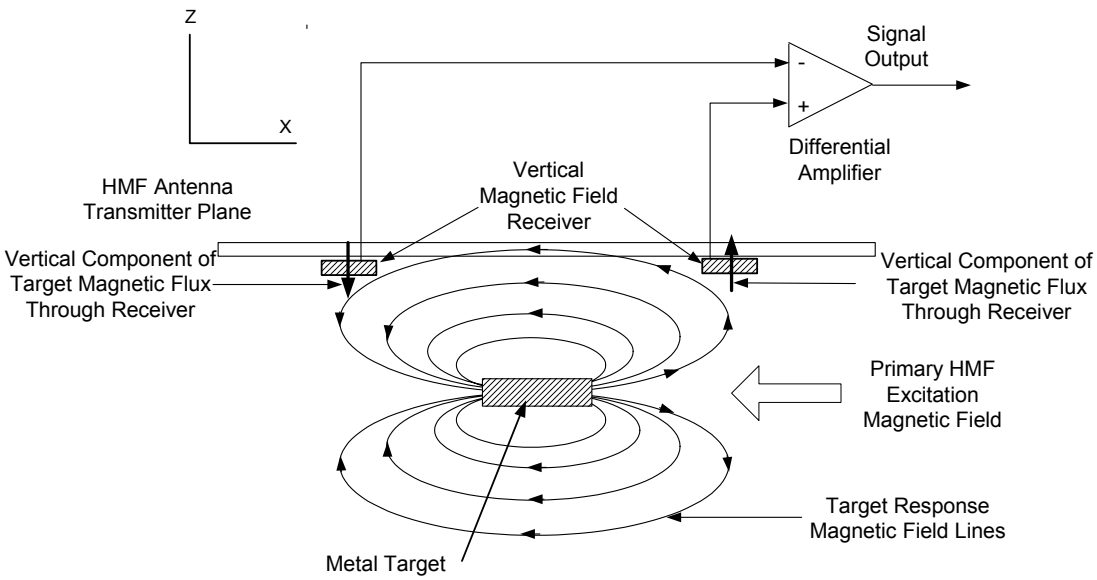

Figure 25 Antenna configuration that decouples transmitter and receiver signals

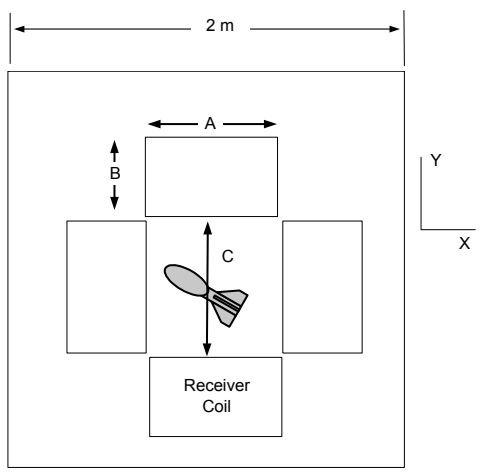

Figure 26 Top view of one proposed receiver loop arrangement.

A JHU/APL-developed MATLAB^{TM} program that models signal response for different antenna parameters was modified for this project. Figure 27 shows a screen shot of the modeling program interface. We modeled the effect of varying the size of the receiver dimensions, A and B, for a fixed C value of 50 cm and a 2 m HMF transmitter. The model excited a dipole target with a uniform and constant HMF. We first investigated whether there was an advantage for a large A value with regard to signal strength fall-off rate. Figure 28 summarizes the results for different values of A, normalized at 20 cm depth. The figure indicates that there is a small advantage in the received signal with large A, but the advantage is not dramatic. Figure 29 shows results for different B values. The rate of increase in signal strength appears to slow as B increases.

Build Sensor: Transmitter & Receiver

Menu and Instructions

Plot Sensor Response

Sensor Details

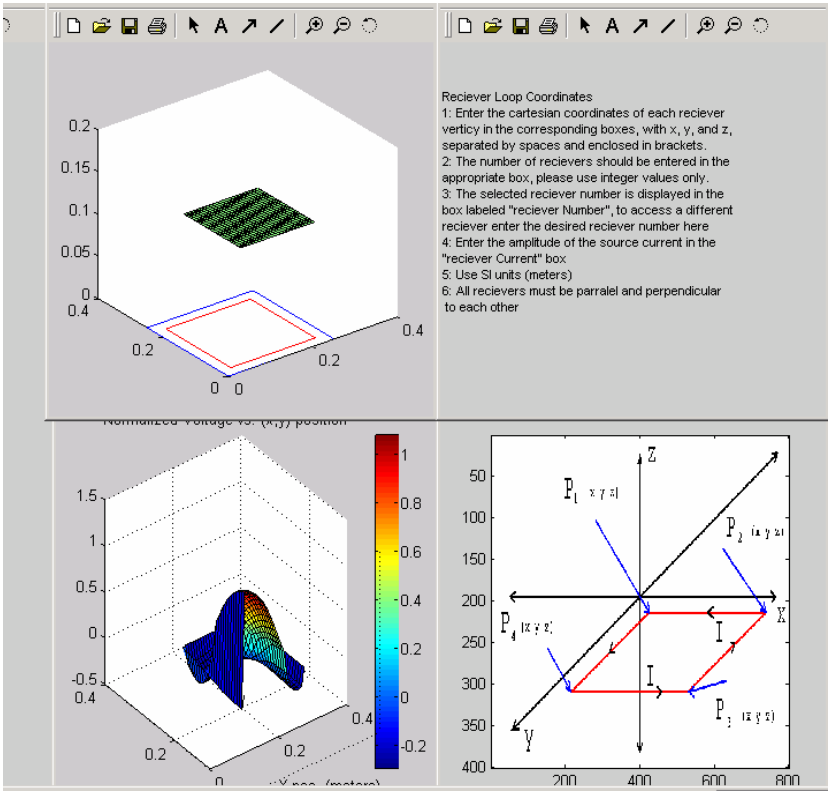

Figure 27 Receiver response modeling software screen shot

For a fixed number of turns, receiver coil inductance increases with coil size. Receiver coil bandwidth is inversely proportional to inductance. Because we would like to have a reasonably wide bandwidth sensor for small target characterization, the receiver size should be made small but still have good signal response with depth. Examining Figure 28 and Figure 29, we have initially selected a receiver that is a square of about 30 cm.

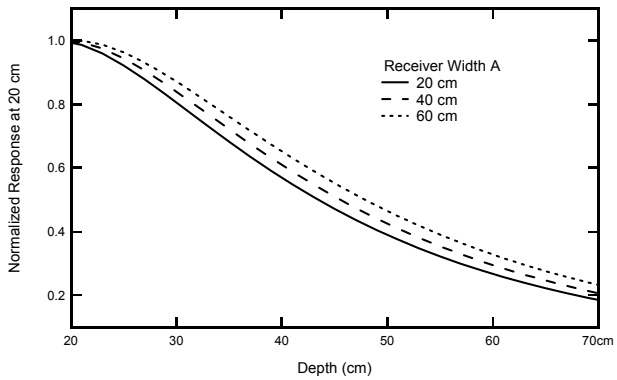

Figure 28 Normalized receiver response for different A values.

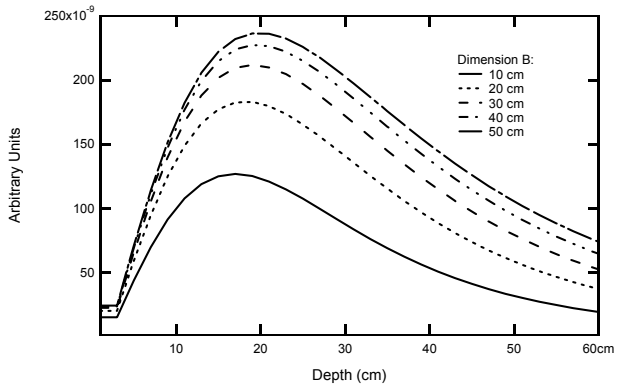

Figure 29 Receiver response for different B values.

We note two interesting observations from Figure 29. First, the output voltage rises to a maximum at about ½ the value of C, the receiver antenna coil spacing as shown in Figure 26. This is a consequence of the geometry of the magnetic flux from the target maximally coupling into the receiver coil at about 20 cm depth. Because we plan to mount the 3DSMF antenna on wheels about 10 cm from the ground, the sensor will have maximum sensitivity for targets about 10 cm deep.

6 FABRICATION AND INITIAL TESTING

6.1 SENSOR SYSTEM FABRICATION

The 3DSMF Sensor System consists of the antenna cart and the electronics cart. The antenna cart is basically a PVC frame with wires comprising the transmitters, receivers, and associated switches. The electronics cart carries the batteries, the power supplies, the DAS, an analysis computer and other test equipment.

Figure 30 shows a simplified block diagram of the 3DSMF Sensor System. A PC/104 computer controls the operation of the sensor system. The computer sends a control signal to the individual antenna power supplies. The amount of current in each antenna element defines the MFV. Once the MFV is set, the computer controls the timing of the electronic transmitter switches and receiver coil analog-to-digital converter operations. Signals from the receiver coils are amplified, digitized, averaged and stored by the computer.

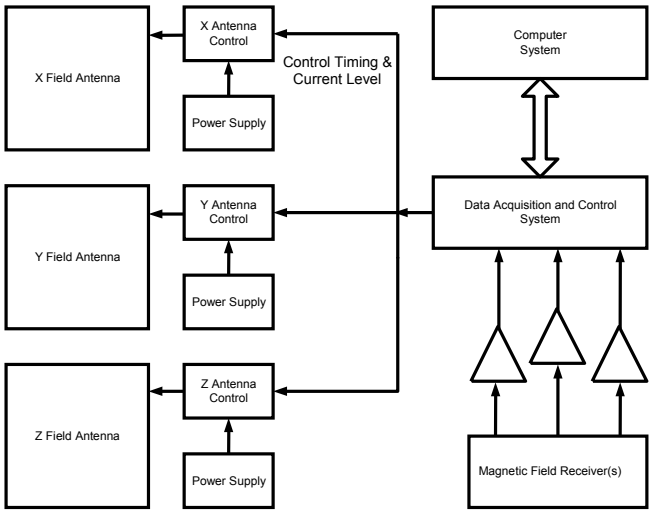

Figure 30 Simplified block diagram of 3DSMF sensor system electronics

The antenna frame is constructed of PVC pipes and fittings, PVC rods and sheet, fiberglass rod, screws and nuts, nylon screws, nuts, spacers, washers, and cable ties, wood sheet, dowels, and boards, certain Delrin® and Teflon® fittings and graphite wheels as shown in Figure 31. The antenna is approximately 2 m by 2 m by 1 m and weighs about 163 kg (360 lbs.) In the figure, the transmitter wiring is red, white, and black. (At the time the photo was taken, other colored wiring was in place for X- and Y-receiver antennas as described in Section 6.3.3.)

The wheel assemblies allow the sensor system to be moved to and around a test site. Both the wheel assemblies and the corner stands are adjustable to allow maximum clearance during transport to a test site and then to allow ground proximity during data collection. Moving the antenna cart between buildings at JHU/APL required more effort than anticipated for a two-person move even though the cart is only slightly heavier than the original design. Therefore, a wood frame has been designed for the base of the antenna to permit towing by a Gator or similar vehicle.

A separate heavy-duty wheeled cart shown in Figure 32 supports the sensor electronics, system batteries, and test equipment. The cabling from the antenna cart to the electronics cart allows a separation of approximately 2.5 m to minimize interference.

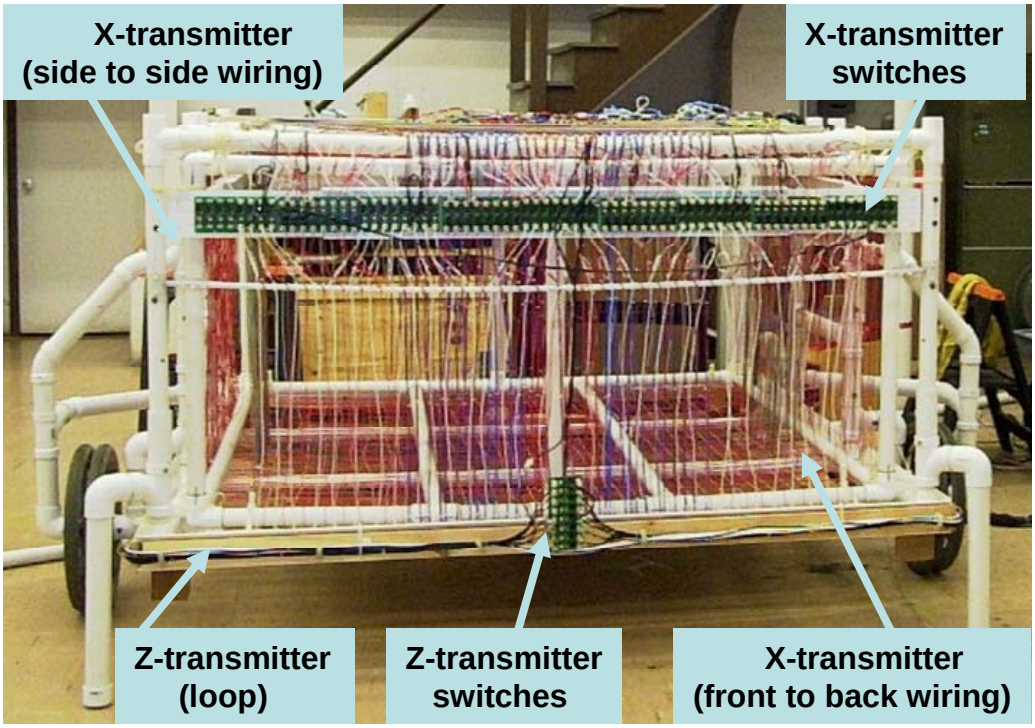

Figure 31 3DSMF antenna cart

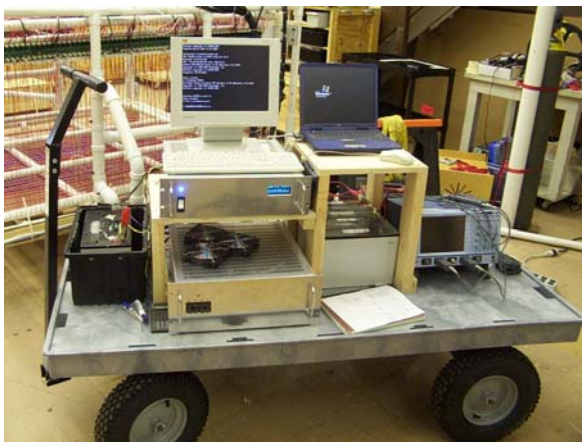

Figure 32 3DSMF electronics cart

6.2 TRANSMITTER CONTROL DEVELOPMENT

To steer the magnetic field in 3D, we control each of the transmitter coil currents to achieve a vector sum MFV by using a lookup table. The lookup table is generated using measured magnetic fields. Figure 33 illustrates target geometry and the MFV reference frame. Figure 34 shows the 3DSMF Sensor System 15º MFVs . In order to realize all the angles shown in Figure 34 we must transmit current in both $X_{forward}$ and $X_{reverse}$ directions.

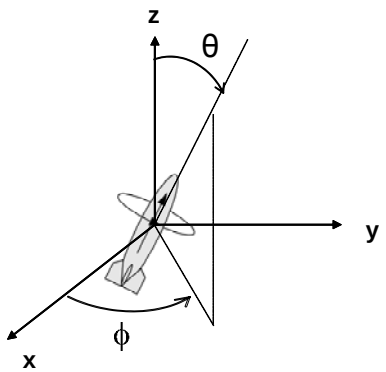

Figure 33 Target geometry

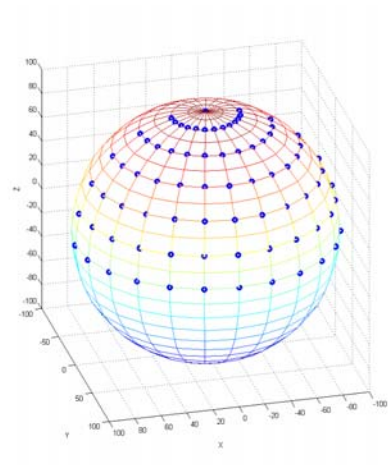

Figure 34 3DSMF 15º MFVs

The initial transmitter configurations were 64 turns for Y (spaced at approximately 2.5 cm) and 32 turns each for $X_{forward}$ and $X_{reverse}$ (spaced at approximately 5 cm). Initial modeling of the X-Y fields predicted that the fields generated for Y versus $X_{forward}$ or $X_{reverse}$ should be well matched.

The pulse operation of the antenna is controlled by the high speed electronic switches operating in parallel. The switches were constructed using MOSFETs in a floating configuration. Opto-isolators were used to couple the switches to the ground-referenced pulse control circuitry. The switches turn off the antenna current in approximately 10 µs (90% to 10% amplitude). Each transmitter coil has two switches to minimize inductance and reduce coupling. A portion of one side of the transmitter switch bank wiring for $X_{forward}$ and $X_{reverse}$ is shown in Figure 35. The second bank of switches is located on the opposite face of the antenna. Some initial testing was done with one switch per turn and one switch per multiple turn, but we opted to implement two switches per turn for this proof of concept demonstration. A future version of the sensor may use fewer switches to reduce the cost and complexity of the system.

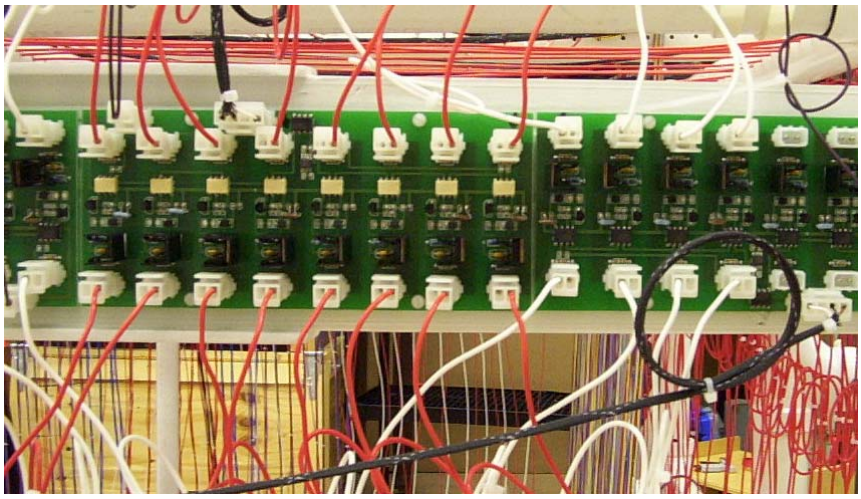

Figure 35 Transmitter switch wiring

Initial testing with the transmitter coils and switches was performed using laboratory power supplies. Measurements with a three-axis magnetometer were taken at 20 cm spacing across the antenna. Figure 36 shows the resulting fields when current is transmitted separately in the X, Y, and Z-directions. In the figure, the magnitude is shown as Volts where 1 V = 10 µTesla.

The main principle of the 3DSMF Sensor System is that the magnetic field is steered into different directions by varying the currents in the individual directional antenna elements. Initially, commercial AC/DC programmable power supplies were proposed for the prototype sensor system. Further developments showed that these power supplies would have restricted the sensor to an AC power source, thereby compromising the portability of the sensor for field testing. To resolve this portability issue, we built voltage-controlled DC/DC converter based power supplies using commercial, high efficiency (~85%) voltage-controlled switching DC/DC converters. Four Second Generation Vicor 24Vin / 12Vout / 400Watts converter modules were used for each of the four transmit channels. Use of the DC/DC converters also entailed minimal thermal management and allowed compact packaging for planned field tests.

The DC/DC converters are adjusted by digital pots which are controlled by the system controller (PC/104) and optically isolated from it. Since all of the switches and coils have fixed serial resistance, the current flows in the coils can be changed in magnitude by changing the voltage that is supplied to the coil. The control signal is multi-wire that includes a serial clock line, a data line, and four chip selects. Sixteen 10k ohm digital pots control the 16 converters.

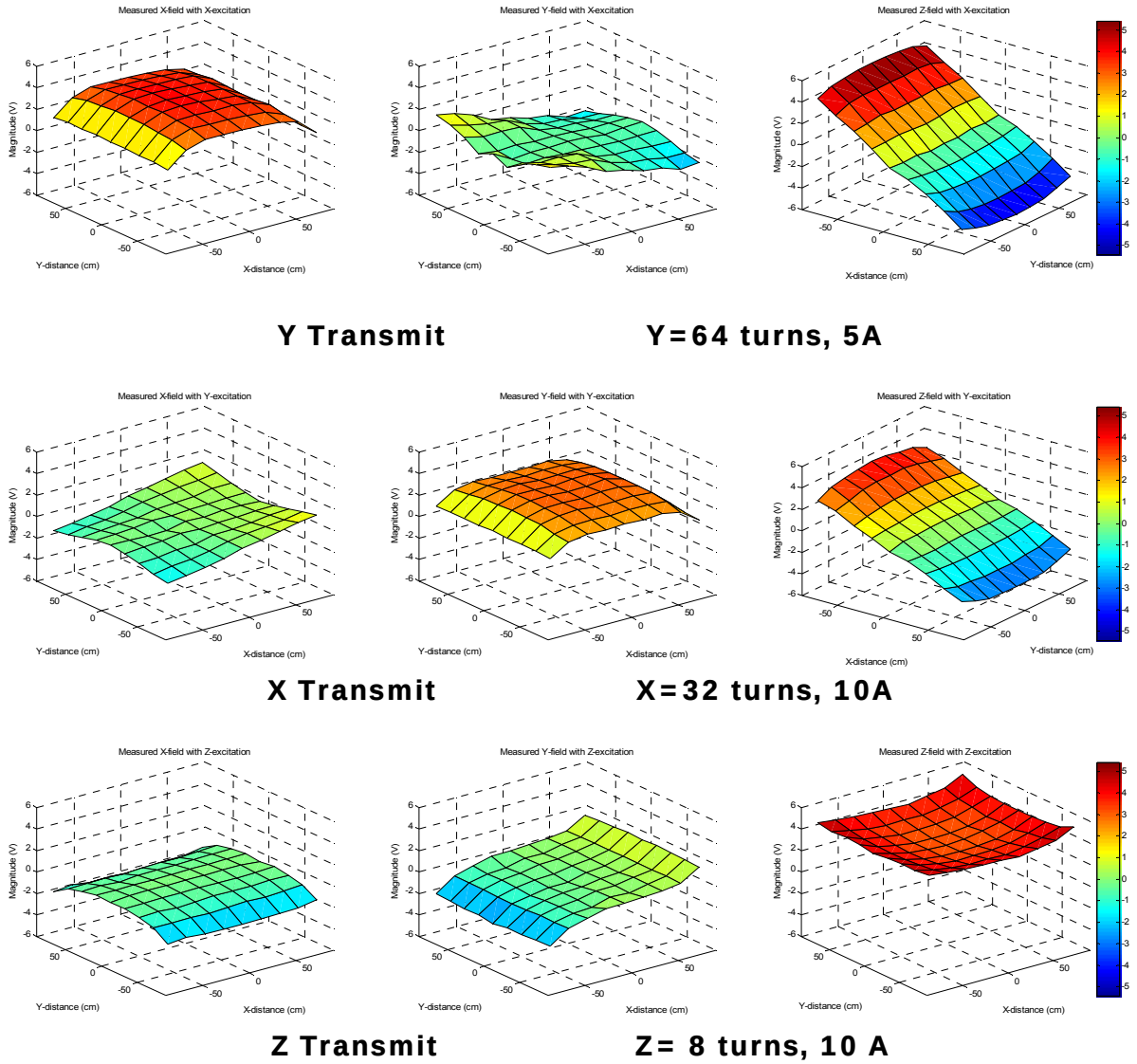

Figure 36 Measured magnetic fields

Although the DC/DC converters cured the portability problems, they created others. The first was startup switching. Initial charging by the converters caused overshoot on the first pulse, as demonstrated in Figure 37 where one trace is approximately 0.2V greater than the others. In this example, the same MFV was repeated 200 times. Relatively minor software changes to ignore data collected on the first pulse mitigated this problem.

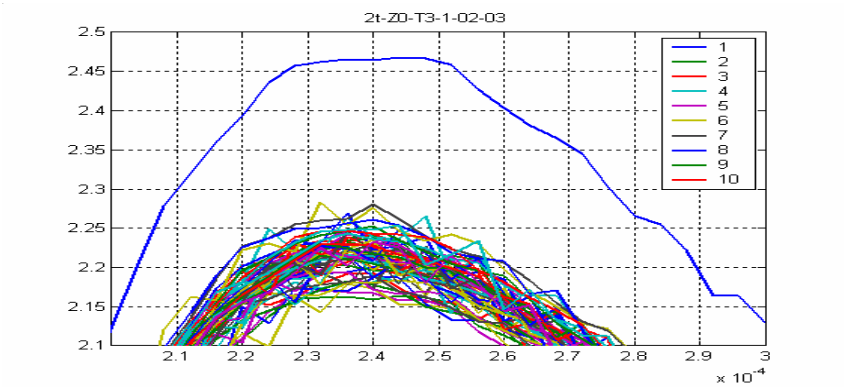

Figure 37 Transmitter startup switching overshoot

The second problem was that the coupling between the parallel $X_{forward}$ and $X_{reverse}$ transmitter wires produced a kickback voltage greater than 600V. The DC/DC converters were not adequately protected against this kickback voltage and so the $X_{forward}$ and $X_{reverse}$ power supplies can not be connected at the same time. Thus data collections were obtained for only half the originally planned MFVs.

The third, and most serious, problem was that the DC/DC converters could not operate over the voltage range specified by the manufacturer in the dynamic fast-switching environment required by the 3DSMF Sensor System. The range was specified to be from 1.2V to 13.2V; however, experiments yielded a range only from 6V to 12.7V. Thus, the transmitters could be electronically steered only through a very limited subset of MFVs.

To solve this problem, we designed and constructed sensor-specific voltage-controlled linear power supplies. While much less efficient than the switching DC/DC converter approach, the linear power supplies have excellent voltage/current control behavior with adjustability in the range from 0.2 to 13 V in 0.1 V steps with short circuit and over current protection.

Figure 38 shows the details of the original DC/DC power supplies and Figure 39 shows the new linear supplies. Some work remains to package the linear supplies for field use after we complete operational testing.

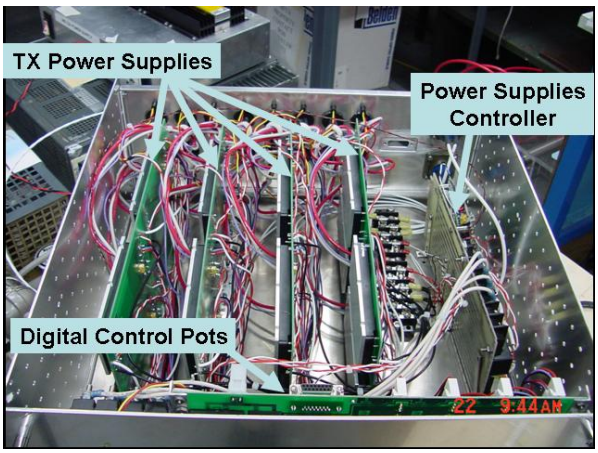

Figure 38 DC/DC converter power supplies

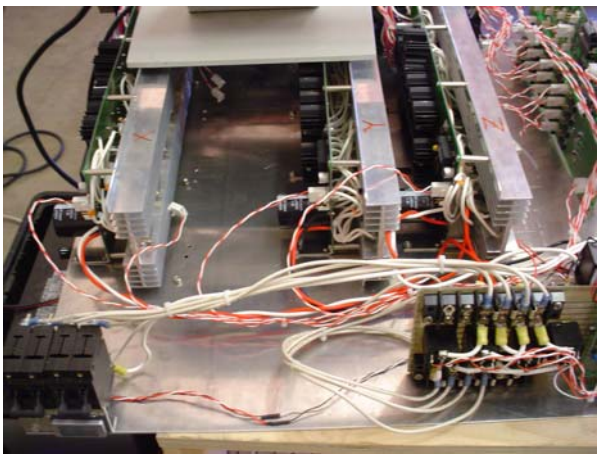

Figure 39 3DSMF linear power supplies

Figure 40 shows the magnetic field strength versus current control values for the two power supply configurations. The DC/DC design is shown with solid lines while the new linear power supplies are shown as dotted lines. In this graph the field strength is measured in volts, where 1V equals 10 µT.

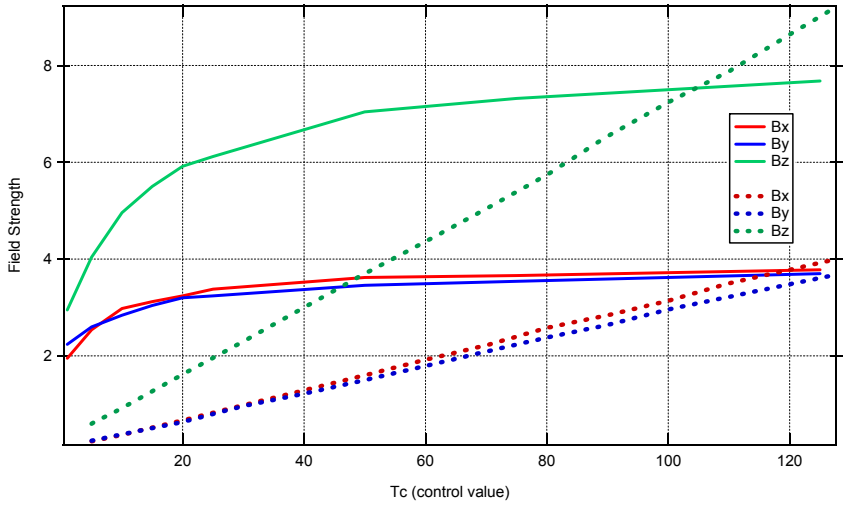

Figure 40 Magnetic field strengths versus control values

6.3 RECEIVER OPTIMIZATION

6.3.1 INITIAL CONFIGURATION

Although a quadrature receiver was modeled, it was not fully implemented. Preliminary testing was performed with a two-element planar summing receiver as shown in Figure 41 (the antenna cart is on its side). The received signal levels were low due to the small size of the coils and the relatively few number of turns in the differential configuration. Rather than continuing on this

path, we instead installed a one meter square loop Z-receiver with 60 turns suspended below the bottom of the transmit plane as the first receiver configuration.

Figure 41 Two-element planar receiver

6.3.2 SWITCHED-COIL RECEIVERS

A problem inherent in the design of basic EMI metal detectors is that the high kick-back voltage of the transmitter coil temporally "blinds" the receiver from amplifying metal target signals near the turn-off time of the transmitter. The transmitter is an impulse excitation to the receiver coil, and as such, the receiver coil has a decay voltage proportional to its inductance. Since receiver coils typically have many turns for increased sensitivity they have relatively large inductances. These large decay voltages can persist for many microseconds and mask the signal from metal targets. In addition, typical kick-back protection circuitry also has a delay time that "blinds" the receiver.

JHU/APL developed and tested a novel method to sense metal signals closer to the transmitter turn-off time compared to conventional coil design [11]. For a given receiver coil configuration, we want the receive coil to be "invisible" during the transmitter turn-off transient. One way to make the receiver coil invisible to the transmitter turn-off transient is to minimize the inductance of the receiver coil during this critical time. We accomplished the receiver coil inductance minimization by breaking the conventional multiple turn receiver coil into individual wire segments so that current is not allowed to flow in a loop during the transmitter turn-off transient. Somewhat inaccurately, but for illustrative purposes, the receiver coil has no inductance (since there is no complete loop formed) during the transmitter turn-off transient. One or more electronic switches are used to form (or connect) wire segments into complete loops to complete the detection circuit for metal signal detection (via Faraday's Law) after the transmitter turn-off transients have decayed to an acceptable level. The inductance of the individual wire segments are in parallel during the transmitter turn-off time and hence, are very small compared to a multiple turn coil (e.g., hundreds of micro-henries).

We developed and tested the necessary electronic design for an ideal switched-coil receiver for landmine detection applications, but funding and time constraints prevented successful implementations for the somewhat different receiver configuration requirements of UXO detection. Although commercial parts are available to quickly build prototype UXO switched-coil receivers, their electrical characteristics are less than ideal because of limited bandwidth. Initial testing has shown improvements in the receiver sensitivity and transmitter/receiver decoupling and the switches are valuable in the 3DSMF Sensor System implementation. One of the receiver switch boards is shown in Figure 42. This switched-coil receiver technology may be useful in other pulse induction EMI metal detector designs such as the EM 61 series of metal detectors from Geonics.

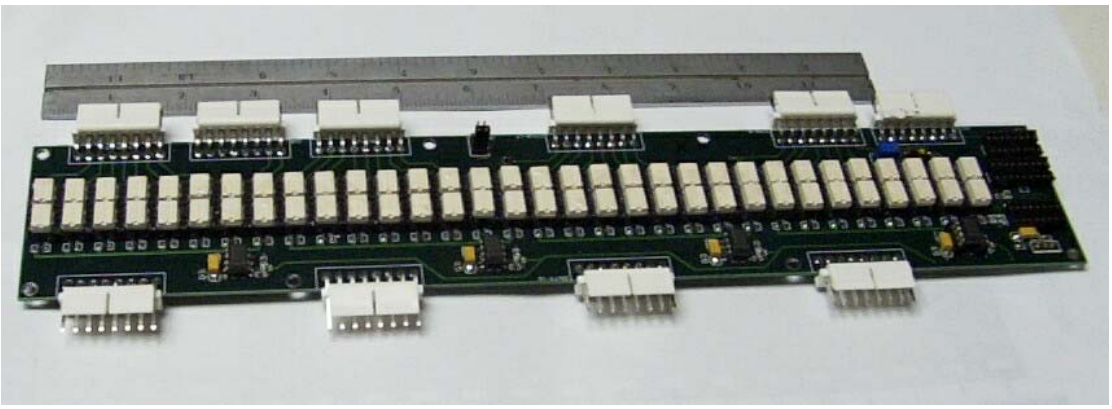

Figure 42 Receiver switch circuit

Figure 43 demonstrates another benefit of the switched coil receivers. These are scope traces of rebar measurements made with the antenna cart resting on the floor. The green trace is the transmitter current and the red and yellow traces are the + and – receiver signals. On the left the receiver is in saturation until after approximately 300 µs. On the right, there is less saturation with the switched coil receiver configuration.

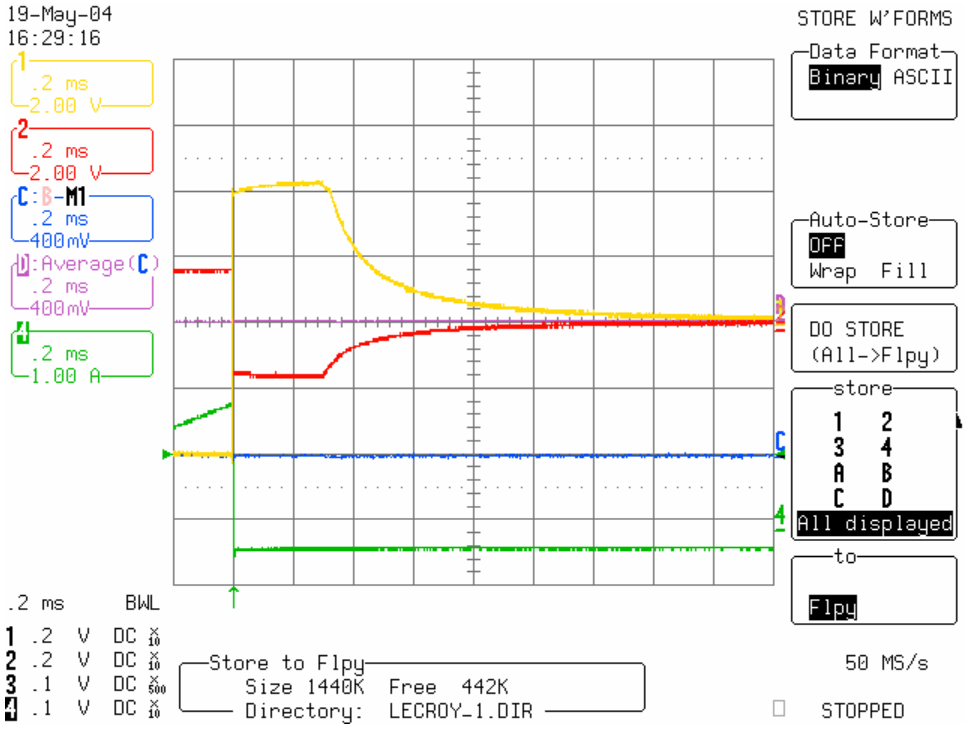

a)

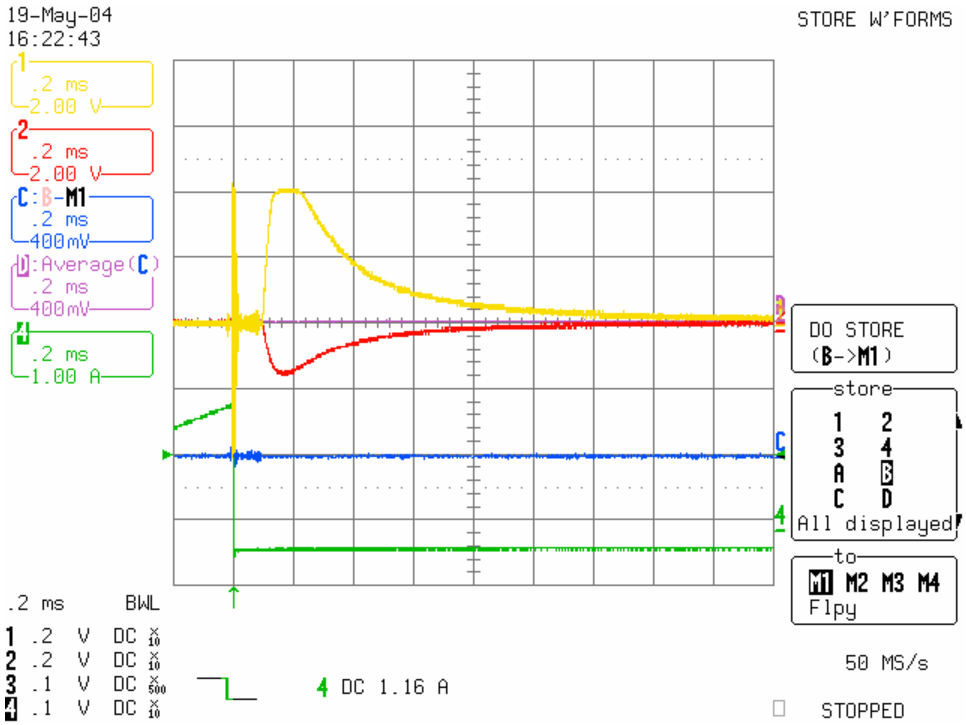

b)

Figure 43 Receiver response, a) no switches and b) with switches

6.3.3 THREE-AXIS RECEIVERS

The data collection system was designed with three receiver channels in anticipation of a future three-axis receiver system. Although modeling indicated that a single axis receiver was adequate for target classification, SERDP and other researchers suggested the addition of a three-axis receiver design could optimize the system. We first quickly implemented and tested a three-axis receiver (as shown in Figure 44) to verify the simultaneous operation of the three receiver channels. For these tests, the target was between the transmit plane and the receiver. We next constructed the 0.6 m cube three-axis receiver coils as shown in Figure 45. This cube was placed inside the bottom center of the antenna cart for testing. Although the receiver sensitivity was low, the test results for this configuration justified further experimentation.

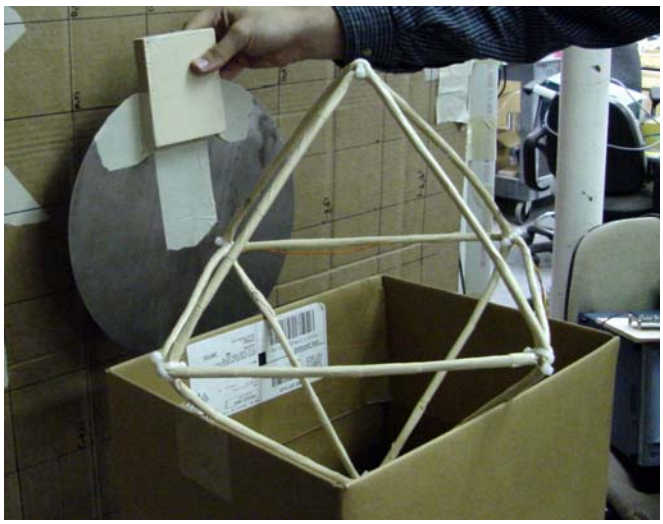

Figure 44 Small three-axis receiver

Figure 45 Three-axis 0.6m cube receiver

Finally we constructed, two large sets of switched X- and Y-receiver coils (1.5 m x 0.8 m x 1.0 m) to supplement the large Z-receiver coil. The X- and Y-receivers were wired with 32 coils of four turns apiece on the X- and Y-transmitter frames. (These coils can be seen in Figure 31 as wires of colors other than red, white, or black.)

During tests of this configuration, 60 Hz pickup and transmitter to receiver coupling (TRC) were two of the most troubling problems. We first tried the standard method of closely matching the data cycle time to a harmonic of 60 Hz and using ensemble averaging to minimize the 60 Hz pick-up. This method appeared to solve the problem, but the 60 Hz signal levels were still close to saturating the high-gain receiver amplifiers.

Steering a transmitter magnetic field in 3D presents special problems for the receiver coils. When a fixed transmitter and receiver coil arrangement is constructed, TRC is constant and a fixed offset can be subtracted from the receiver signal. With the 3DSMF generator, the transmitted field constantly changes direction and the receiver coils have a constantly changing TRC. Ideally, the coupling would be constant for each MFV and a look-up table could be used to subtract a previously measured coupling signature. The problem with this approach is TRC

needs to be very stable over time and temperature to measure the target signatures accurately. A second issue is that the receiver amplifiers go into saturation during the transmitter turn-off pulse and time signature measurements near the transmitter turn-off time are lost. This is primarily due to the high inductance of the large, multiple turn receiver coils. As an aside, the TRC issue is one reason a TD metal detector is preferred over a FD version for the 3D antenna. The variable TRC is expected to be more difficult to resolve in a FD sensor.

The process of receiver optimization presented a number of other interesting problems. One anomaly manifested itself as intermittent system noise as illustrated in Figure 46. The oscillation shown was traced to loop back when the AC power supply which charged the 12V system batteries inadvertently remained connected during measurements.

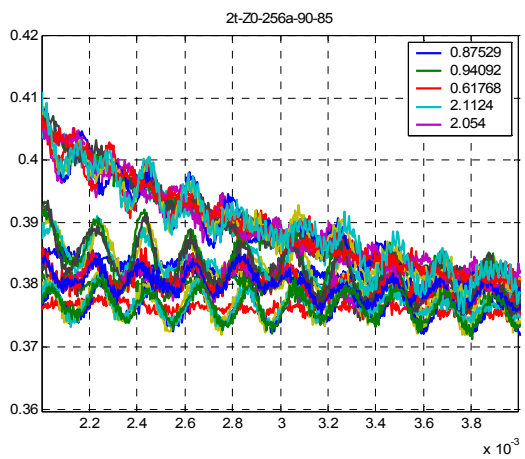

Figure 46 Illustration of system noise

6.3.4 DIFFERENTIAL CONFIGURATION

We spent many weeks attempting to get the three antennas working. Due to funding and schedule issues, the decision was made to focus on a working Z only receiver coil. The fastest and easiest solution to minimize 60 Hz pickup and TRC was to use a differential coil arrangement. A second Z receiver coil was mounted to the top of the antenna cart as shown in Figure 47 and produced a factor of 20 (26 dB) reduction in 60 Hz pickup (which was sufficient for the measurements). Additional techniques could be used to reduce the 60 Hz noise, but they would require time consuming firmware changes. This balanced receiver coil technique works well for minimizing the transmitter decay current and offers an additional benefit of far-field noise cancellation. Each 1.5 m by 1.5 m Z-receiver consists of 30 turns of 18 AWG hookup wire mounted on a thin sheet of plywood.

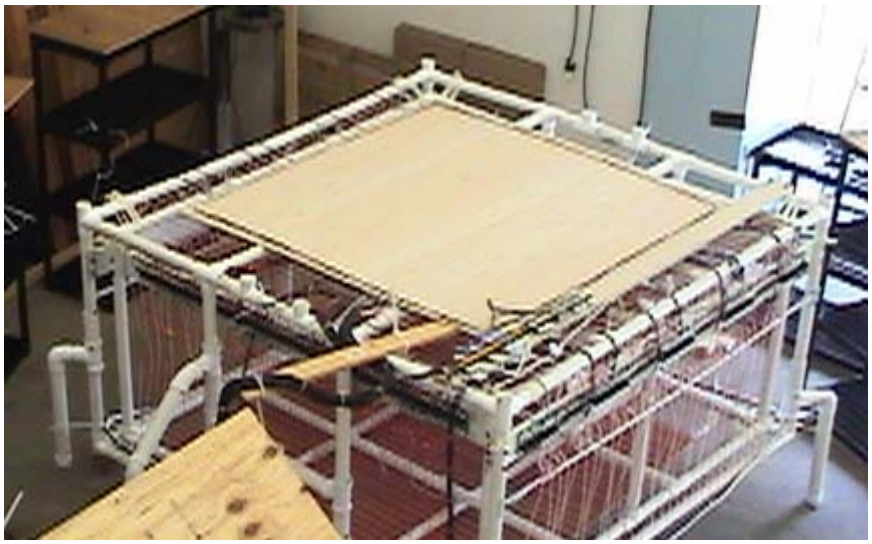

Figure 47 Top view of secondary differential Z-receiver coils

6.3.5 RESIDUAL COMPENSATION

The switched, differential receiver coil configuration does not completely eliminate the TRC. Although the remaining signal is only a few tens of millivolts (compared to as much as several hundred volts), the receiver channels have a gain of 1000 and this residual TRC still causes some saturation of the receiver amplifiers. Several methods were investigated to compensate for the residual TRC:

- Bucking coils
- Injected signals
- Digital compensation

A 20 cm square bucking coil (up to 160 turns) was constructed and placed between the Z-transmit and Z-receive coils. This configuration was only moderately successful because the bucking coil picked up environmental noise and injected it into the system. We also used a programmable waveform generator to inject signals to compensate for the coupling but had difficulty with the presence of ground loops. This concept could possibly work very well but it would require the design and development of an opto-isolated programmable waveform generator. If this approach is pursued, more work would also be needed to design and integrate appropriate signal generators, summers, filters, etc. A more promising solution might be implementation of digital compensation by means of dynamic sample/store subtraction circuit with feedback which is similar to the injected signal compensation technique just described.

6.4 DATA ACQUISITION SYSTEM (DAS) DEVELOPMENT

A computer DAS based on the PC/104 standard (IEEE-P996 Standard) performs data acquisition, control, data storage and display functions. The computer controls the analog-to-digital converter (ADC) board operation, pulse repetition rate of the transmitter, transmitter current, data averaging, and data display. Figure 48 shows a block diagram of a wireless Ethernet implementation of the DAS using a web-based approach to system control and data

collection. For laboratory data collection we replaced the wireless connection with a hardwired link to a laptop PC.

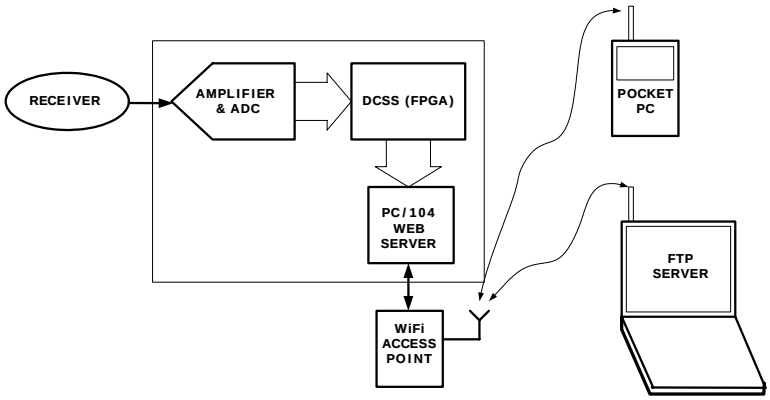

Figure 48 Wireless Web-based data collection approach

The 3DSMF DAS technology was derived from a JHU/APL-US Army project which developed the Electromagnetic Target Discriminator (ETD). Figure 49 shows the two ETD web windows that are used to control the operation of the sensor system. The majority of the control software was developed using C code. The web-based approach to data control and data collection allows a level of flexibility that was not possible a few years ago. The user accesses the data collection system via any web browser by inputting the address of the sensor. In the parameter window, the user selects the digitizing sample rate of the sensor and the number of scans to ensemble average per MFV. The acquisition window allows the user to set the file name for the data collection. When all parameters are set, the user presses 'Acquire' and the data is collected and recorded. The number and direction of the MFVs that the sensor collects is software controlled. Theoretically, a researcher could collect field data from his desktop computer many miles from the field test site from many different data collection systems.

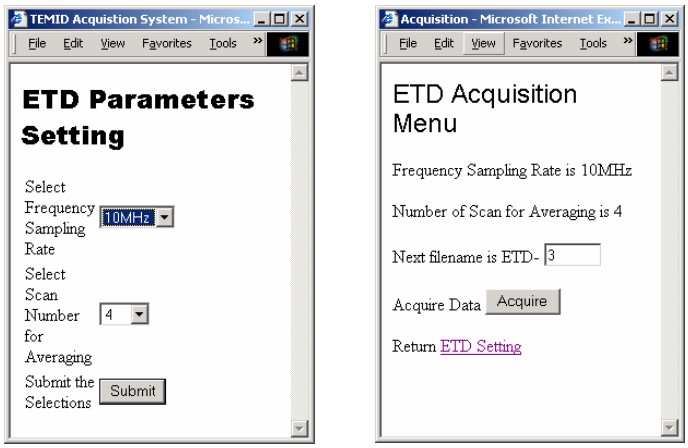

Figure 49 Screen shots of ETD data collection and control computer interface

The ETD sample frequency is selectable from 50 kHz to 5 MHz and the ensemble averages are selectable from 4 to 512. Table 1 presents the data collection times (including fixed data transfer

overhead) for various sample rates and ensemble averages. At 250 kHz, data collection takes about three minutes per target for the full set of MFVs shown in Figure 34.

Table 1 3DSMF Data Acquisition Time

Data Collection Time (s) for 15º MFAs				
Sample Frequency (Hz)	**# of Averages**			
	64	**128**	**256**	**512**
50k	109	213	420	834
100k	58	109	213	420
250k	27	47	89	172
500k	16	27	47	89
1M	11	16	27	47
5M	7	8	10	14

Three data collection subsystems (DCSS) were implemented to collect signals from the three magnetic field receivers. Each DCSS consists of an XSA-100 prototyping board from XESS, an isolation board and an amplifier/ADC board.

The XSA-100 (shown in Figure 50) houses a Xilinx SpartanII XC2S100-field programmable gate array (FPGA), 16 MByte synchronous DRAM and 256 KByte Flash. The FPGA controls the operation of the ADC and performs data averaging at each MFV. The FPGA has 40 K Block RAM for fast access, 100,000 system gates, 600 Configurable Logic Blocks, and operates at 100 MHz. The advantages to using the inexpensive, commercial off-the-shelf XSA-100 were ease of development and its small foot print. Minor disadvantages were found to be that many pins were shared with different components causing conflicts during program development and that unused components draw power and cause electrical interference.

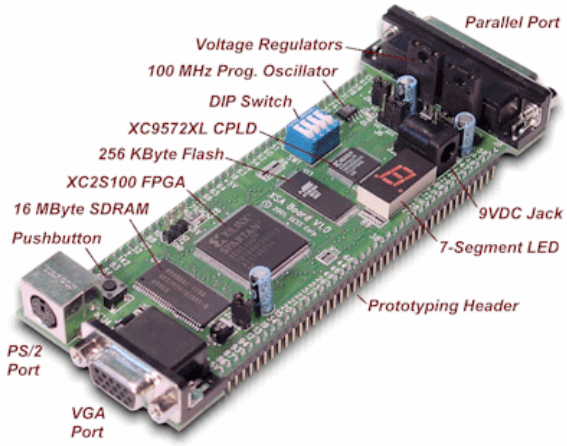

Figure 50 XSA-100 prototyping board

Figure 51 shows the isolation board which facilitates programming of the FPGAs by disconnecting the signals from the rest of the system to the XSA-100 board.

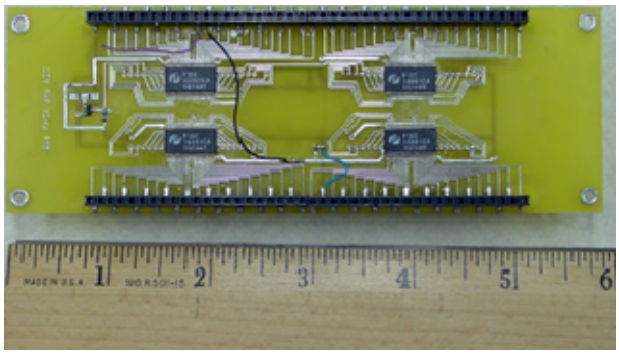

Figure 51 DCSS isolation board

The amplifier and data collection systems were based on high-speed metal detector technology that was developed to classify fast decaying metal targets indicative of low-metal landmines. In order to keep SERDP development costs low, we reused most of the electronic designs developed for the landmine project. High-speed amplifiers and high-speed ADCs are inherently electrically noisy compared to low-speed electronics. Future electronic designs of the 3DSMF sensor system would use low-noise components and low-noise electronic design configurations.

The amplifier and ADC boards were designed using Orcad Layout Plus for standard surface mount components and consist of five layers: the top components and traces, a positive power plane, the ground plane, a negative power plane, and the bottom traces. The receiver amplifiers have a total fixed gain of 1000V/V consisting of a low noise 1st stage for 100V/V and a 2nd stage of 10V/V with a differential driver to the ADC. The low-power (250 mW), 14-bit, ADC has a maximum sampling rate of 10Ms/s. The board is shown in Figure 52.

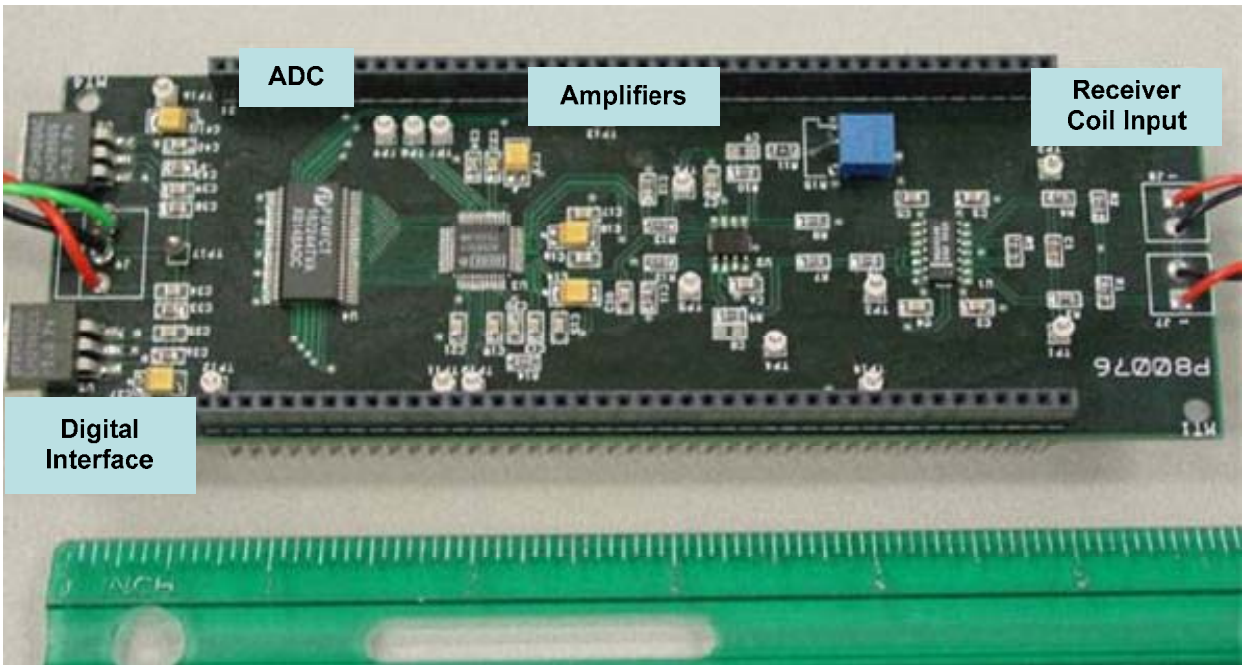

Figure 52 Amplifier and ADC board

The micro controller was designed with a standard PC/104 architecture using the following components (as shown in Figure 53):

- PPM-520 - AMD SC520 CPU operating at 133 MHz
- PCM-UIO96A - Universal 96-Point I/O with Interrupts
- PCM-FPVGA - High-resolution, video controller

With this design, the data can be archived for later processing and the software and be migrated to another PC/104 system with minimal changes.

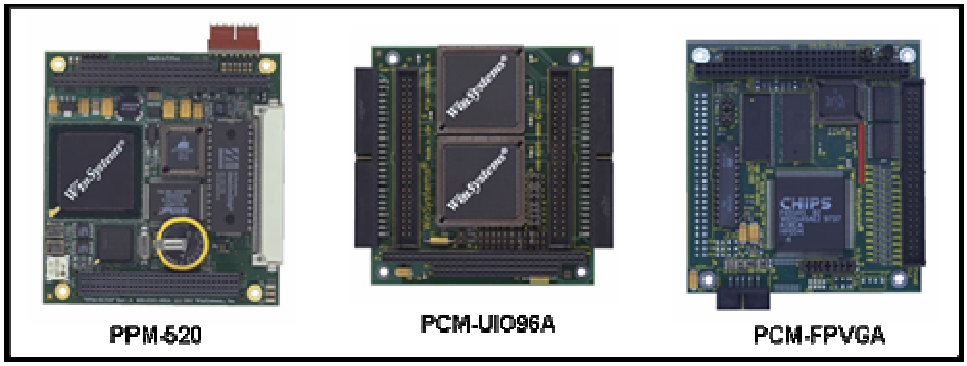

Figure 53 DAS PC/104 components

The interface to the DAS is either a computer with an internet browser and installed FTP server or a pocket PC with WiFi such as the HP iPAQ h5550 as shown in Figure 54.

Figure 54 HP iPAQ h5550 Pocket PC

Figure 55 shows preliminary test results of the DAS electronic noise with the amplifier input shorted. The RMS noise level with four ensemble averages is about 0.7 mV. A power spectral density (PSD) analysis of the noise shows that the dominate noise source appears to be 1/F noise typical of the wide-bandwidth high speed amplifiers we are using in the receiver circuit. Low noise amplifiers would be considered in future designs.

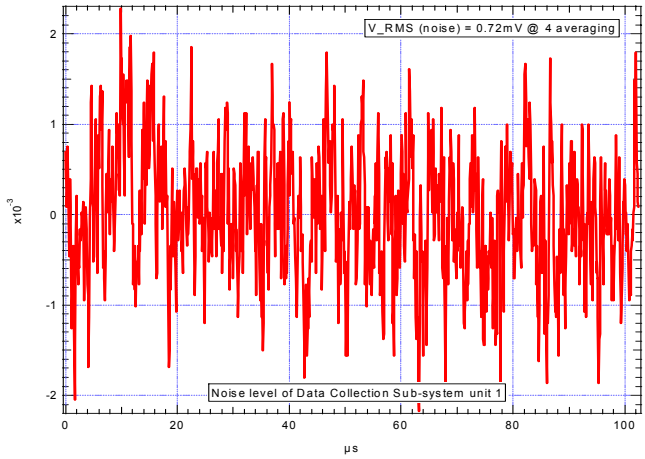

Figure 55 Noise level of DAS amplifier and ADC.

Figure 56 shows sample test data from the DAS system using a high bandwidth test receiver coil and a small piece of steel scrap a few inches from the antenna plane. The target decay signal was digitized at 5 Ms/s and the data collected over a 200 µs time window. Each data scan is 1024 points. A 60 point binomial filter was applied to the data shown in the figure. The receiver coil comes out of saturation at about 15 µs. The figure shows the receiver electronics have approximately four orders of dynamic range.

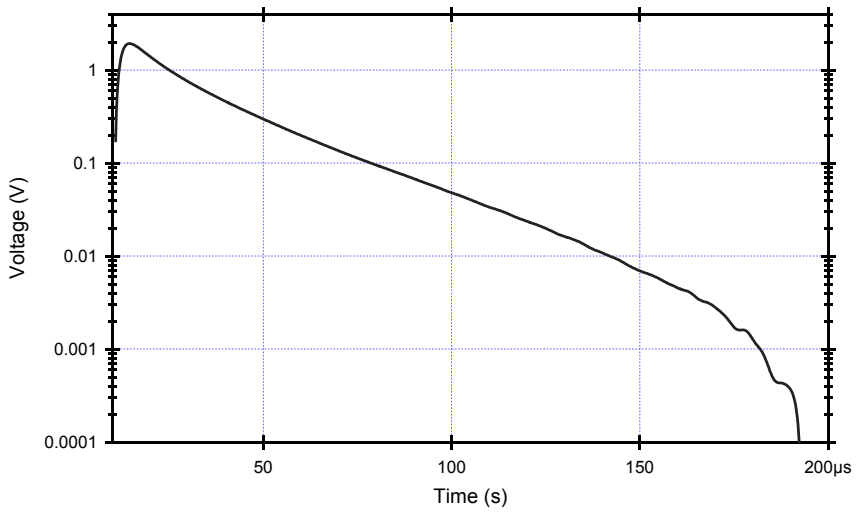

Figure 56 Sample data from receiver electronics

Figure 57 shows the interior of the DAS and telemetry enclosure.

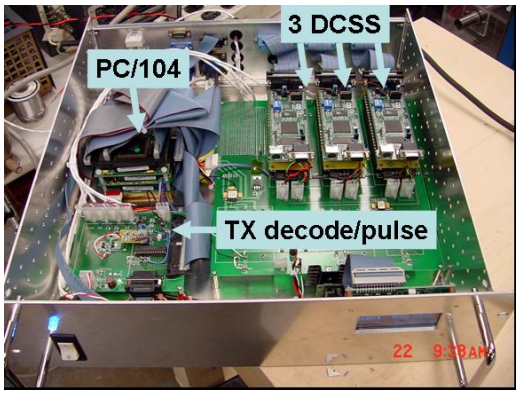

Figure 57 Interior picture of DAS and telemetry system hardware

The DAS presented a problem during the process of testing the time and temperature stability of the transmitters and receivers. The problem was manifested by the appearance of "banding" in the target signatures as shown in Figure 58. Repeated measurements of the same target at a single MFV yielded results which fell into discrete bands of values. The magnitude of the differences between the bands was sufficient to compromise the assessment of target orientation.

The target signature banding took several weeks to resolve. We basically took apart the system looking for the source of the problem: background measurements (external sources), transmitter electronics, transmitter coils, receiver coils and switches, steering current control, receiver amplifiers, and analog to digital converters (ADC). We finally traced the source of the problem to timing jitter of a few microseconds in the ADC command signals. Initially, a timing jitter of a few microseconds was thought to be inconsequential because the data collection window is hundreds of microseconds wide. However, eliminating the timing jitter in a single receiver channel resolved the target signature banding problem for that channel. The solution was to select one DCSS sample clock as the 'master' to trigger all data acquisition. The other receiver channels are configured as 'slaves'.

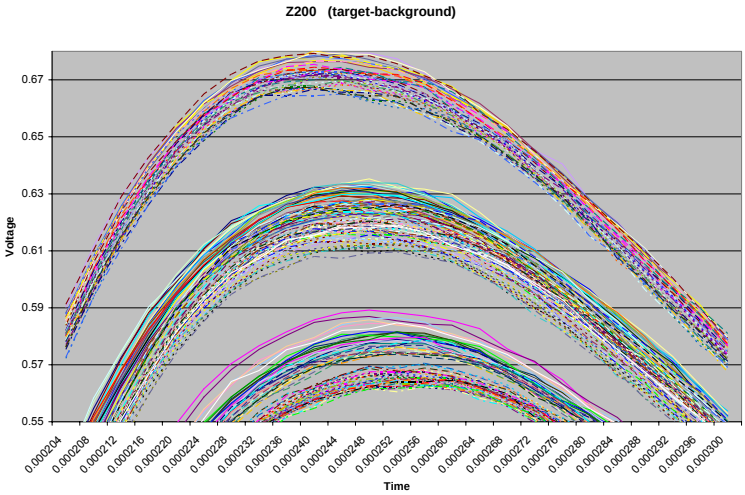

Figure 58 Example of target signature banding due to timing jitter in DCSS.

6.5 INITIAL LABORATORY TESTING

Rebar in the concrete floor (interfering metal signal) makes it necessary to raise the 3DSMF antenna cart off the floor a distance of 1.4 to 1.7 m (54-66 inches). In one JHU/APL laboratory the cart is suspended by a ceiling hoist while measurements are made. In other laboratories a fork-lift is used to place the antenna cart atop heavy-duty plastic shelves which are cross-braced with pieces of 2 x 4 wood. Figure 59 shows the 3DSMF Sensor System in test position using the hoist. Targets are placed on the plastic stand under the antenna in the appropriate orientation and at the desired distance from the antenna cart.

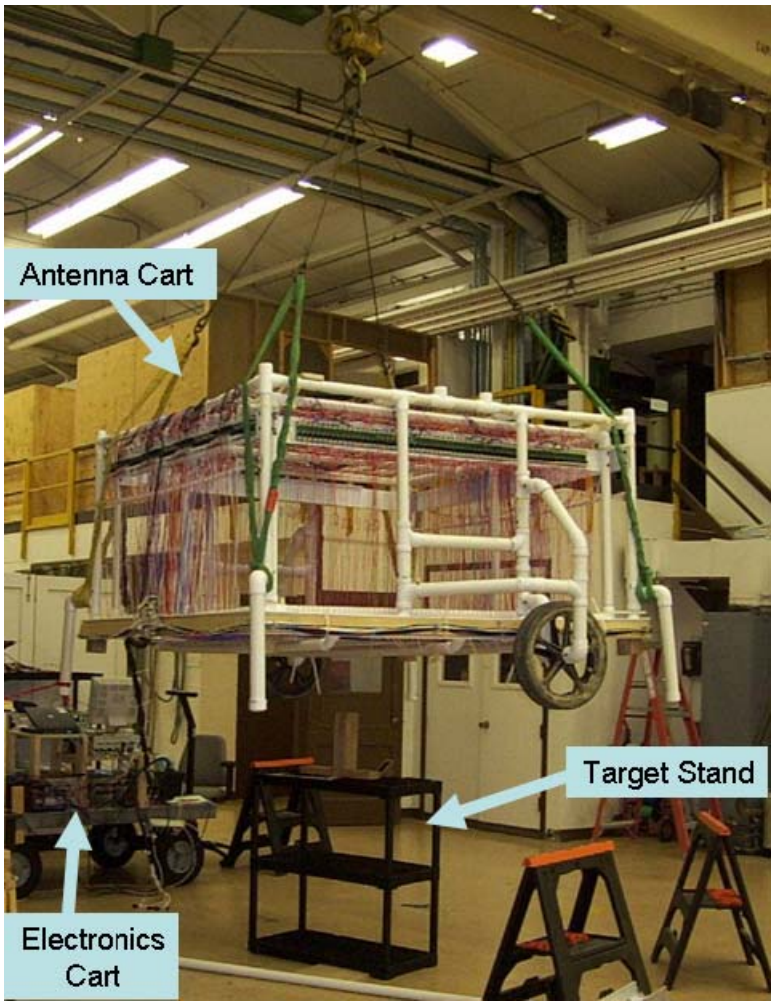

Figure 59 3DSMF antenna in laboratory test position

A simple calibration ring and other calibration targets were fabricated or obtained for initial laboratory testing to solve problems which arose during the system integration as discussed above. This testing has produced data collection standards and methodologies which were used in subsequent laboratory testing.

7 2005 ACTIVITY

During 2005, the project focus was:

- Investigating several different magnetic field receiver configurations to detect all components of target response
- Validating system design using simple calibration targets such as wire loops and a metal sphere
- Collecting data from more complex targets such as pipes
- Analyzing data of complex target responses to determine target identification and orientation

7.1 FINAL 3DSMF ANTENNA CONFIGURATION

7.1.1 TRANSMITTERS

The original design for the 3DSMF consisted of 64 turns for the Y-transmitter matched to 32 turns each for $X_{forward}$- and $X_{reverse}$- transmitters. The final configuration of the transmitters is 32 turns for both $X_{forward}$- and Y-transmitters. The Z-transmitter is 15 turns. As discussed in Section 6.2, the $X_{forward}$- and $X_{reverse}$- transmitters cannot be connected simultaneously so this $X_{forward}$-only configuration "illuminates" ¼ of the hemisphere.

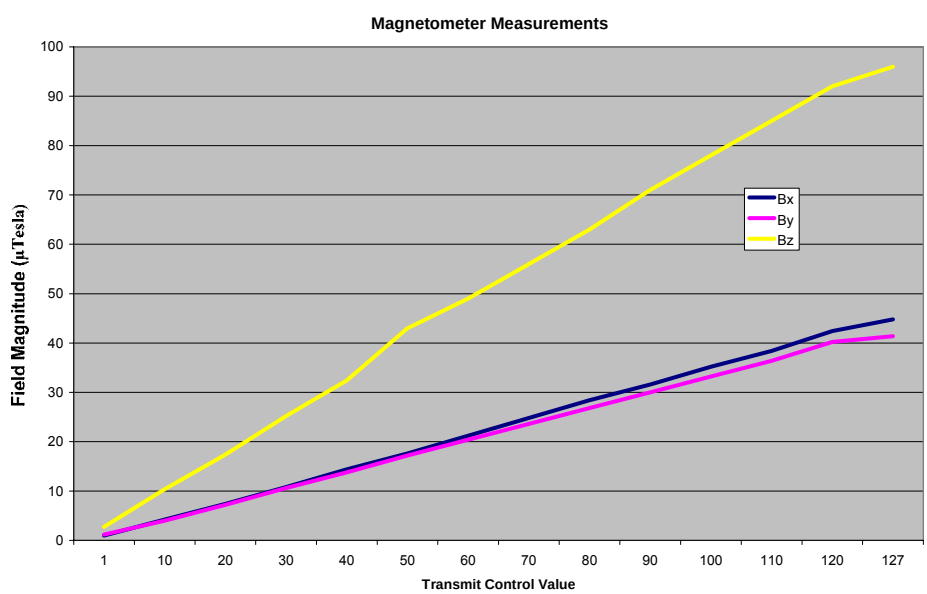

Figure 60 Magnetic field magnitudes for varying X-Y-Z transmit control values

Figure 60 illustrates the magnetic fields measured at a distance of 12 inches below the transmitters as the transmit control values are varied across their dynamic range. This data is used to equalize the maximum transmissions for the X-Y versus the Z-channels and to construct a matrix of control values in order to generate the MFVs similar to those shown in Figure 34.

7.1.2 RECEIVERS

A significant challenge of this project has been to devise and fabricate a receiver system to adequately and accurately measure the multiple components of target response. As described in Section 6, the evolution of receiver strategy included an original quadrapole concept, a series of 3D configurations, and a loop Z-only implementation. Analysis of data from the loop Z-only receiver showed promise in resolving the components of target MPVs for target identification and determination of target orientation as long as the target was not situated in the XY-plane.

To mitigate the XY-plane blind spot, we returned to the original design concept of using X- and Y-quadrature receivers as shown previously in Figure 25 and Figure 26. These quadrature receivers are not only larger (18 in. square) than the initial implementation described in Section 6 but consist of more turns. The result is that the bandwidth of the present design is not as large as originally intended.

The final dimensions and placement of the receivers is shown in Figure 61. The outer Z-coil and each of the paired X- and Y-coils are 10 turns.

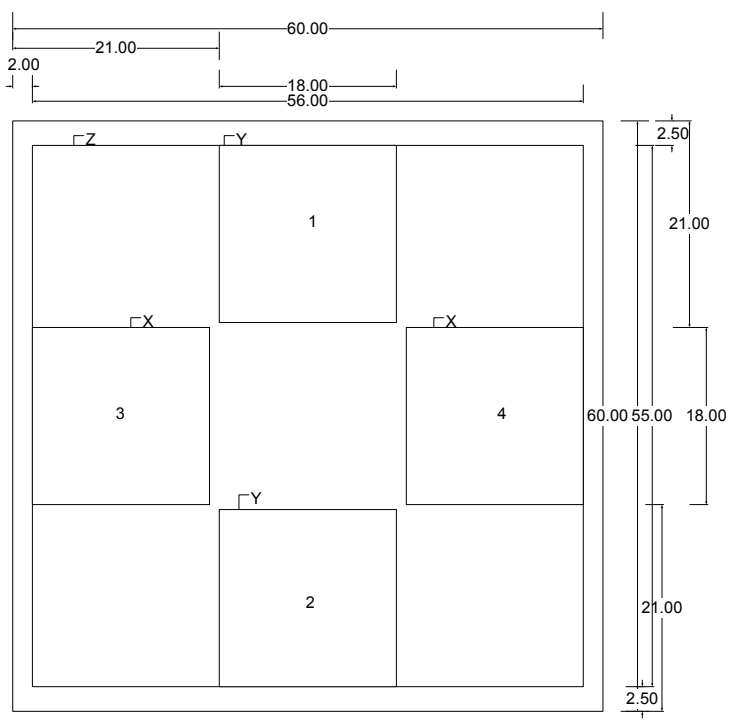

Figure 61 Final 3DSMF receiver configuration

The intrinsic differences of the transmitters (loop Z versus X-, Y-HMF generators) and receivers (loop Z versus some other configuration for X-Y) introduce complications for analysis of data from unknown targets at unknown depths. We experimented with several X-, Y-receiver configurations and with variations in the number of Z-receiver coils. Target data integrity was verified with measurements with and without the X-Y receivers present.

7.2 DATA ANALYSIS

The following analysis involved characterizing the time decay responses for different calibration targets (coil, sphere, and pipe). The sphere and coil data were used to measure the differences among the X-, Y-, and Z- channel receiver responses to determine normalization constants. And the known time decays of the coil and pipe data were used to test whether or not the orientation of the object could be determined from responses collected on the X-, Y-, and Z-receivers.

For targets with strong responses, the receivers are still in saturation up to 200 μsec after transmitter turn-off. For the calibration targets studied, the signal decayed to the noise floor of the receivers by 1600 μsec. Therefore for automated processing of this data, all signals were windowed between 240 to 2000 μsec. After some experimentation these were found to be good cutoff points. This window is a variable which could be adjusted if the specific UXO targets expected to be found at a particular site had significantly different eddy current decay responses.

Using the pipe rotated in the XY-plane as a simple example, the longitudinal and transverse time decays were calculated with the pipe and transmitted field oriented as in Figure 62.

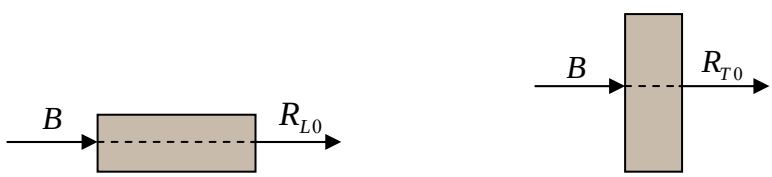

Figure 62 Longitudinal and transverse responses

Then with the pipe oriented at some φ, as shown in Figure 63 the responses were recorded for the X-receiver channel after X-only transmit and for the Y-receiver channel after Y-only transmit. For maximum transmit on X-only, the expected X-receiver response equals

$$R_x^{x-xmit}(t,\varphi) = P_L^{x-xmit}(t)\cos(\varphi) + P_T^{x-xmit}(t)\sin(\varphi)$$

where

$$P_L^{x-xmit}(t) = R_{L0}(t)\cos(\varphi) \qquad P_T^{x-xmit}(t) = R_{T0}(t)\sin(\varphi)$$

and for maximum transmit on Y-only, the expected Y-receiver response equals

$$R_y^{y-xmit}(t) = P_L^{y-xmit}(t)\sin(\varphi) + P_T^{y-xmit}(t)\cos(\varphi)$$

where

$$P_L^{y-xmit}(t) = R_{L0}\sin(\varphi) \qquad P_T^{y-xmit}(t) = R_{T0}\cos(\varphi)$$

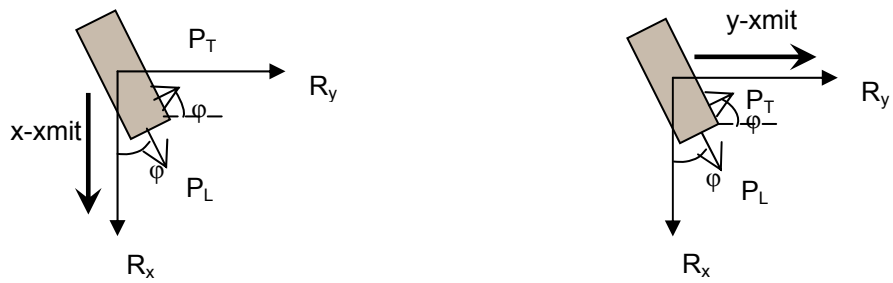

Figure 63 Geometry for φ responses

The pipe orientation is then found by finding φ which minimizes the difference between the measured and expected responses.

7.2.1 X-, Y-, & Z-CHANNEL RESPONSE

Responses from the X-, Y-, and Z-channels were measured using received signals that were collected with an object oriented along a particular axis and with maximum transmit on that same axis. For example, the signal received on Y was measured by orienting an object in the Y-direction and then transmitting only along the Y-axis. The measured differences among the channels remained consistent across different data collection dates and for different objects.

The transmitters and receivers are identically configured for the X- and Y-channels. However, there is a known gain resistor mismatch in the receiver amplifiers. The relationship between the received signals on X and Y was found to be:

$$m_y(t) = f(m_x) \approx 1.4 m_x(t) .$$

Both the Z-channel transmitter and receiver are fundamentally different than those for the X- and Y-channels as described above. The relationship between Y and Z was estimated using the sphere and coil data:

$$m_y(t) = f(m_z) \approx c(d) m_z(t)^{1.03} .$$

Where $c(d)$ is a variable that is a function of the object distance from the bottom of the antenna. Using the sphere data taken at depths from 2 to 24 inches (to top of sphere), the amplitude ratios characterizing the relationships between the different channel responses were calculated and are shown in Figure 64. This plot shows that the Y to X ratio remains relatively constant with depth, but that the Y to Z ratio decreases linearly with increasing distance.

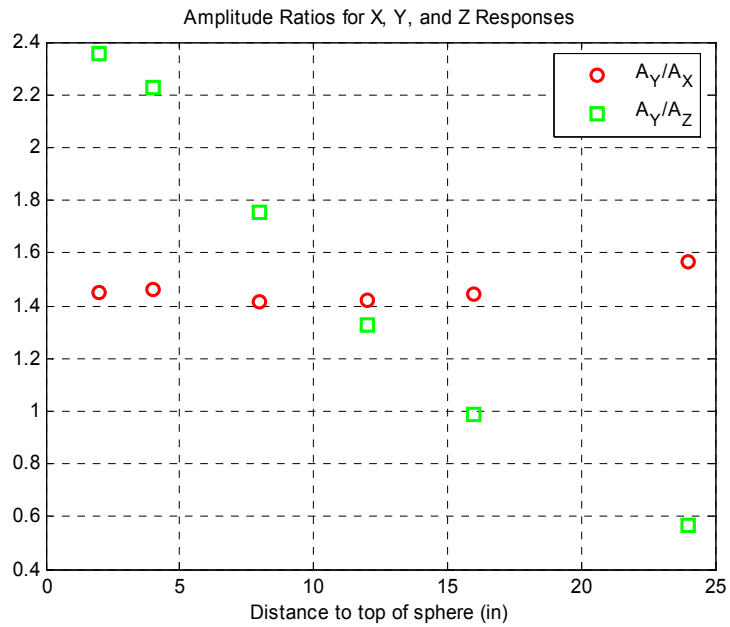

Figure 64 X-Y-Z receiver amplitude ratios for sphere

The time decay ratios characterizing the relationships between the different channel responses were also calculated and are shown in Figure 65. This plot shows that the Y to X τ ratio remains relatively constant between 2 and 12 inches to the top of the sphere, but that the Y to Z τ ratio is about the same value between 2 to 8 inches to the top of the sphere.

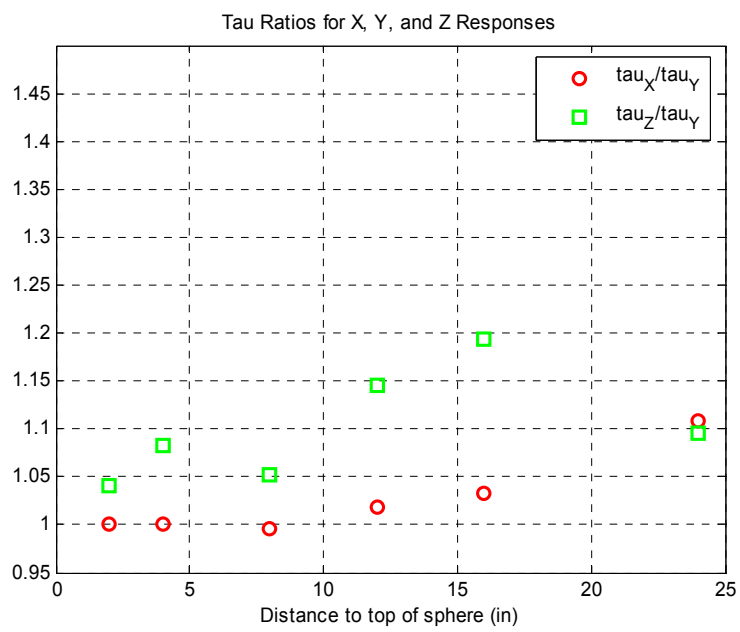

Figure 65 X-Y-Z time decay ratios for sphere

7.2.2 TIME DECAY CONSTANTS

Time decay constants were calculated for three different objects: 1) a wire loop, 2) a metal sphere, and 3) a metal pipe.

Background signals, b_n (n = 1,2,…,N), were collected with no object beneath the antenna and target signals, t_n, were collected when an object was centered under the antenna and oriented along a single axis while the maximum field was transmitted along that same axis. These signals (typically repeated N = 3-10 times during one run) were used to calculate time decay constants of different objects. The following process was used to find the time decays and constants associated with each object (assuming orientation along the y-axis):

1) Extract target signal data, t_n, corresponding to maximum transmit along the Y-axis
2) Extract background signal data, b_n, corresponding to maximum transmit along the Y-axis
3) Filter each target and background signal using a15-tap FIR filter with normalized cutoff frequency of 1/8 (using MATLAB 'fir1.m' and 'filtfilt.m' functions)
4) Subtract background from target signal $r_n = t_n - b_n$ for each n
5) Truncate r_n from samples 60-400 (240-1600 μsec)
6) Fit exponential function $r_fit_n = \sum_i C_{ni} \exp(-t/\tau_{ni})$ to each r_n
7) Calculate the means $C_i = \frac{1}{N}\sum_{n=1}^{N} C_{ni}$ and $\tau_i = \frac{1}{N}\sum_{n=1}^{N} \tau_{ni}$ to obtain the fit
8) For the pipe, normalize exponential function to equal 1 at t = 240 μsec

The wire loop and metal sphere each were found to have one time decay associated with them. The metal pipe was found to have two time decays associated with the transverse and longitudinal responses of the pipe. In addition, both the longitudinal and transverse time decays were best estimated by double exponentials (i = 2).

Initially, time decay constants were calculated for the wire loop and metal sphere. For these cases, visual inspection of the actual (filtered) signal vs. the curve fit showed that a single exponential was sufficient for estimating the decay response as shown in Figure 66 and Figure 67.

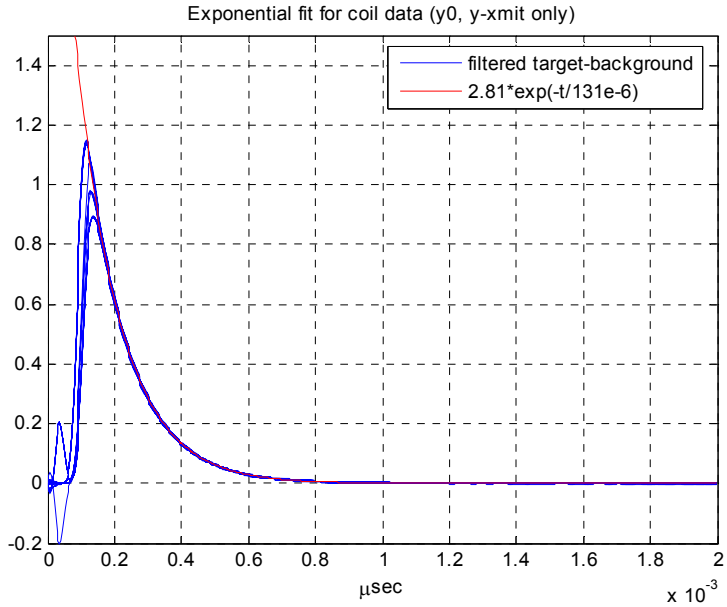

Figure 66 Exponential fit for coil data

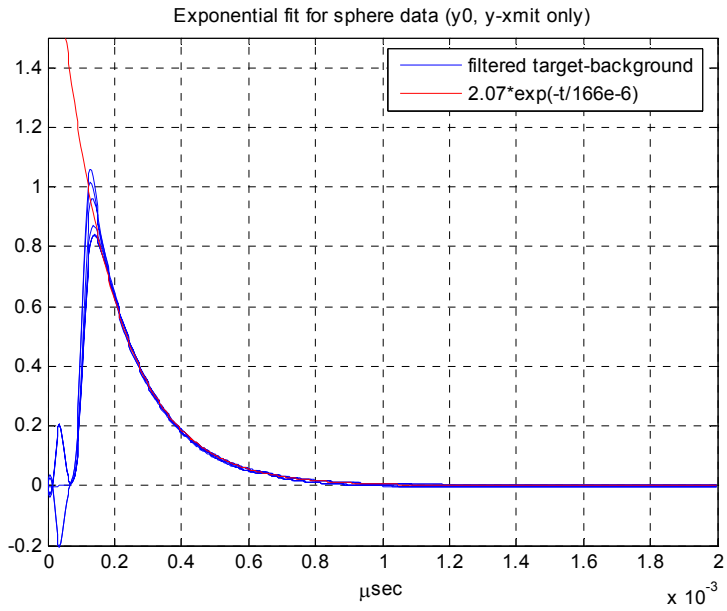

Figure 67 Exponential fit for sphere data

However, there was a large error between the measured data and calculated fit when trying to characterize the pipe data as a single exponential. Therefore, a double exponential was used to model the pipe data. Figure 68 and Figure 69 show that the double exponential is a much better fit for both the transverse and longitudinal responses of the pipe. The signals in these figures were normalized to equal 1 at 240 μsec. The fitted data follows the measured data starting around 200 μsec even though the curve fit was only applied to the windowed data starting at 240 μsec.

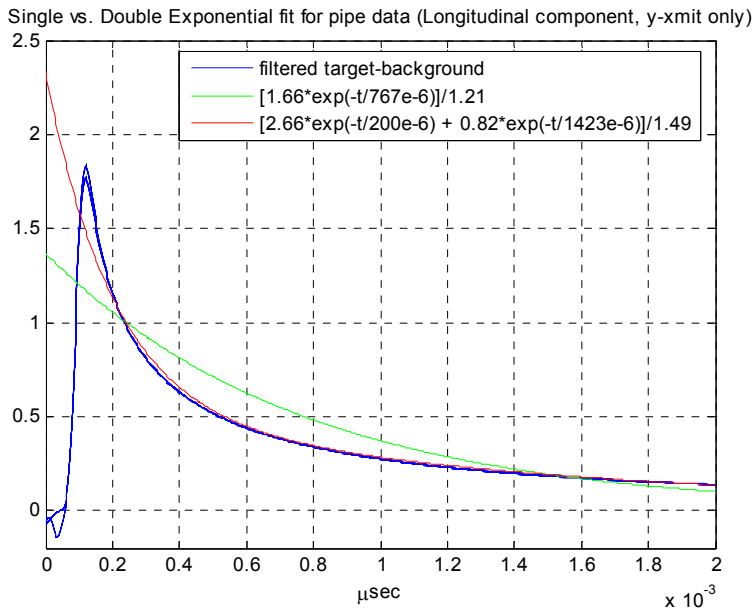

Figure 68 Longitudinal exponential fit for pipe data

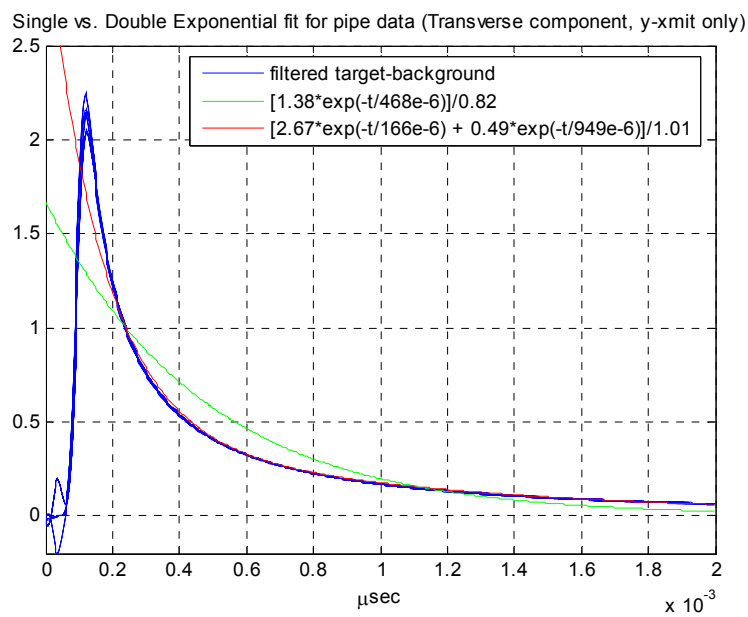

Figure 69 Transverse exponential fit for pipe data

Table 2 lists the measured time decay constants and associated decay responses for the three objects when the distance to object's center of gravity was approximately 12 inches. The theoretical decay constant for coil is 138 μs; the theoretical decay constants for the sphere and the pipe are unknown.

Table 2 Calculated Time Decays

Object	Time constants (μsec)		Decay Response
	mean	variance	
Coil (c138) [N_{total}=20]	131	1.39E-12	$C_1\exp(-t/\tau)$ [C_1=2.8]
Sphere [N_{total} =6]	166	9.90E-13	$C_2\exp(-t/\tau)$ [C2=2.1]
Pipe (p3) [N_{total} =30]			
Transverse	τ_1: 166 τ_2: 949	3.64E-12 2.88E-10	$C_3\exp(-t/\tau_1) + C_4\exp(-t/\tau_2)$ [C_4/C_3 = .18]
Longitudinal	τ_3: 200 τ_4: 1423	1.48E-12 1.18E-10	$C_5\exp(-t/\tau_3) + C_6\exp(-t/\tau_4)$ [C_6/C_5 = .31]

The constant ratios given in Table 2 for the transverse and longitudinal components of the pipe are needed to determine orientation; consequently one concern was that the ratios would change with distance from the antenna. Data was collected with the pipe at depths of 12, 16 and 20 inches and the ratios were checked for a dependence on depth. Figure 70 and Figure 71 show the ratio differences between depths of 12 and 20 inches. For this analysis, it is assumed that these differences are small enough that the time decays calculated while the objects were at 12 inches can also be used to calculate object orientations up to distances of at least 20 inches.

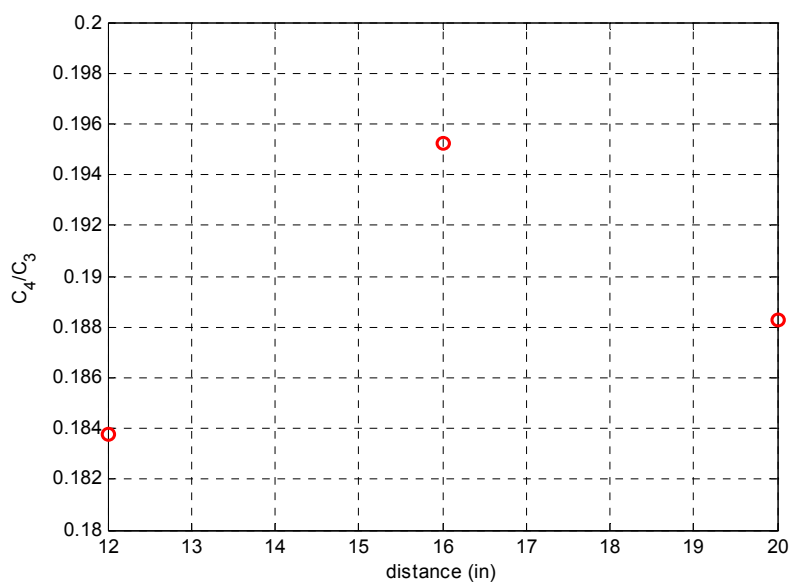

Figure 70 Ratio of pipe transverse amplitude constants with depth

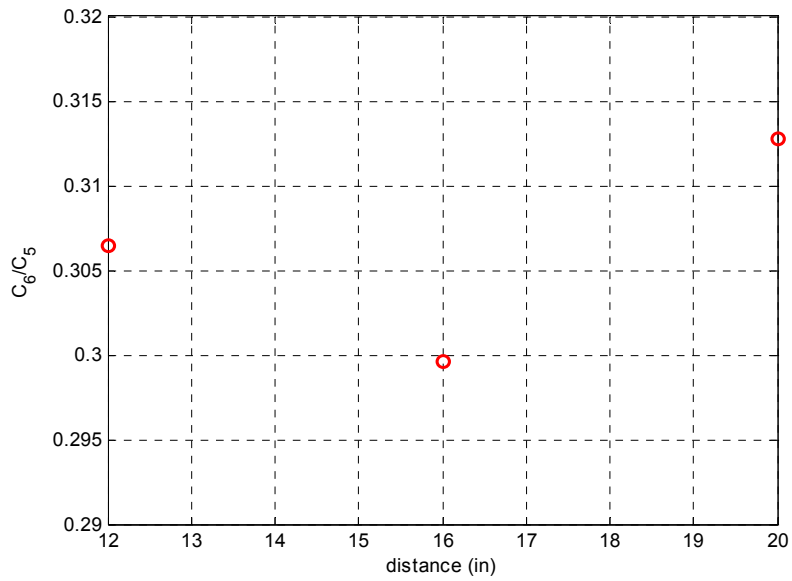

Figure 71 Ratio of pipe longitudinal amplitude constants with depth

7.2.3 TARGET ORIENTATION

The coordinate system for this analysis is shown in Figure 72. The angle φ represents a rotation in the XY plane and θ represents rotation from the Z-axis. So if the X-axis is used as the reference, θ = 90 and φ = 0 correspond to the X-axis.

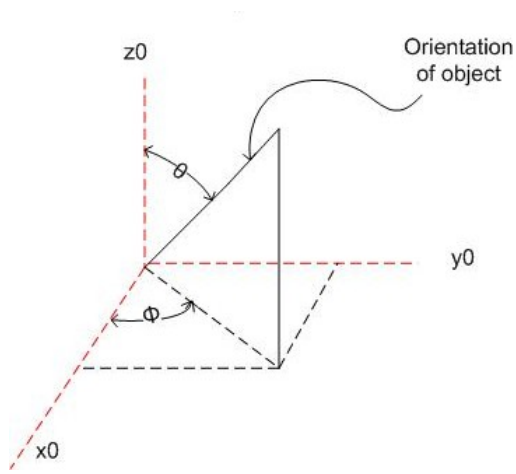

Figure 72 Target geometry for analysis

This analysis assumes that time decay constants of objects are available in a library, but the orientation of the object is unknown. Given the known constants, the expected magnetic field is calculated at different object orientations using equations (8) through (14) in Section 4.

$$U(\phi,\theta) = U(\phi)U(\theta) = \begin{bmatrix} \cos\phi & -\sin\phi & 0 \\ \sin\phi & \cos\phi & 0 \\ 0 & 0 & 1 \end{bmatrix} \begin{bmatrix} \cos\theta & 0 & -\sin\theta \\ 0 & 1 & 0 \\ \sin\theta & 0 & \cos\theta \end{bmatrix}.$$

The steps for finding object orientation are as follows:

1. Using different possible object (φ,θ) pairs, calculate the expected fields on X with the steering vector oriented along the X-axis using equation (1) (then the same for the Y-axis and Z-axis). This creates the possible responses depending on (φ,θ)
2. Extract the signals from the measured data corresponding to what was received on X during maximum transmit on X (…Y during maximum transmit on Y and …Z during maximum transmit on Z)
3. Subtract the measured signal on each channel (X, Y and Z) from all possible (φ,θ) responses for the corresponding channel
4. Average each difference signal to get one measure of the error for X, Y and Z at all (φ,θ) combinations
5. For each (φ,θ) calculate the sum of the squared differences on X, Y and Z.

The object orientation is determined by finding the (φ,θ) that minimizes the values found in Step 5.

7.2.3.1 Coil Analysis

The coil can be characterized by a single time decay constant which is given in Table 2. Data was collected by positioning the coil at different orientations and recording the receiver responses on the X-, Y-, and Z-channels. Equation (1) was used to calculate the expected responses for possible θ_o and φ_o values. The magnetic field, m(t), was calculated for all possible combinations of θ_o and φ_o in one degree increments between 0 and 90 degrees. Then the orientation of the coil was determined by finding the θ_o and φ_o that minimized the squared differences between the calculated and measured responses. The results are shown in Table 3 where the undefined angles are designated as "xx."

The surfaces in the following figures are the squared differences of the calculated and measured θ_o and φ_o for several coil orientations. The results show that measuring responses while transmitting on X-only, Y-only, and Z-only are enough to determine the coil orientation. In general, the measured positions were within 9 degrees of the nominal or actual positions

Table 3 Actual vs. Measured Coil Position

Target Orientation	Nominal φ	Calculated φ	Nominal θ	Calculated θ
X0	0	6	90	90
Y0	90	90	90	90
Z0	xx	xx	0	0
XY45	45	47	90	90
XYZ45	45	46	45	39
XZ45	0	9	45	39
YZ45	90	90	45	40

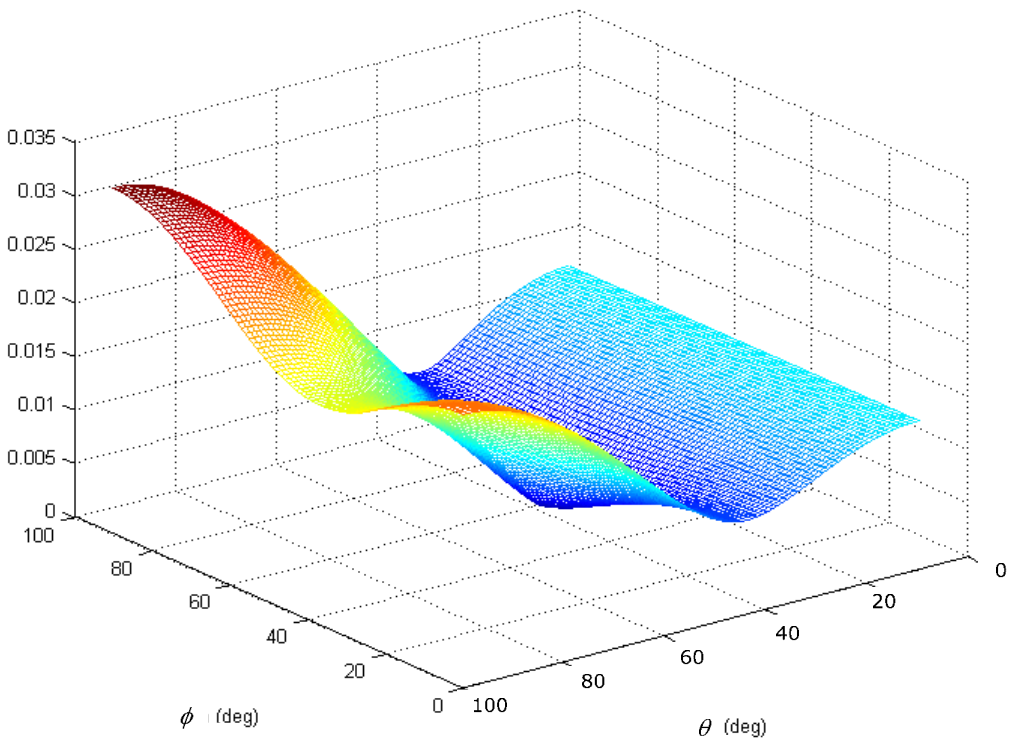

Figure 73 Position: XYZ45, Measured Position: ,φ= 46, θ = 39

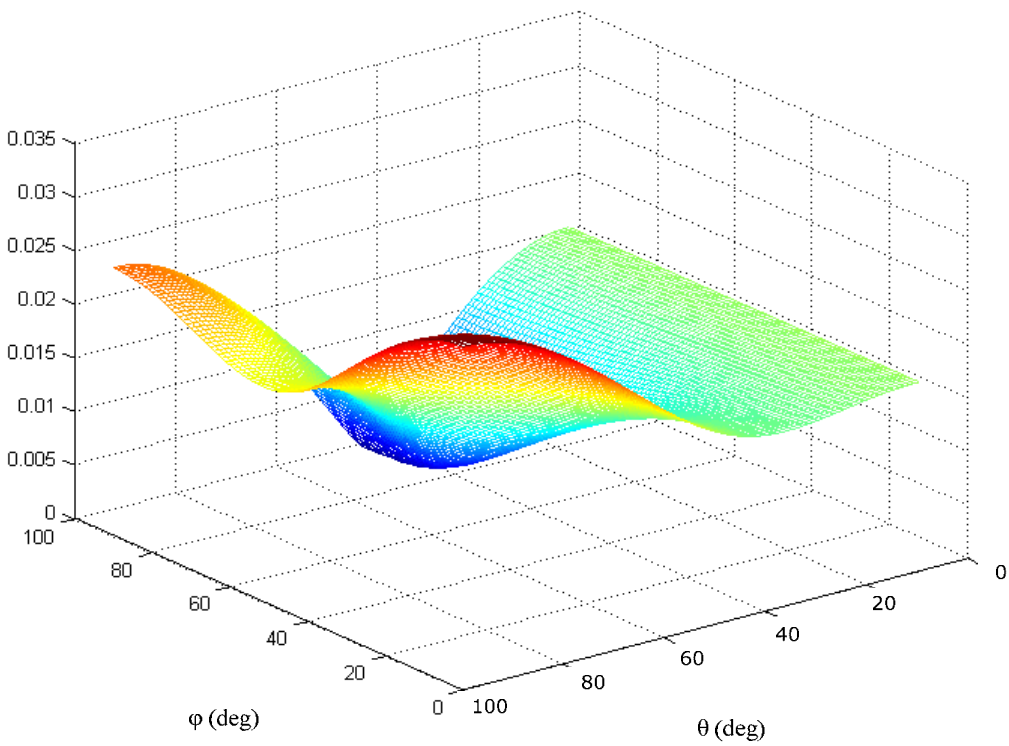

Figure 74 Position: YZ45, Measured Position: ,φ = 90, θ = 40

7.2.3.2 Pipe Analysis

The pipe is an axially symmetric object and has eddy current time decay components in both the longitudinal and transverse directions. The time decay responses for both directions are represented by double exponentials and are given in Table 2. Data was collected for the pipe at different orientations and the responses were measured on the X-, Y-, and Z-channels. Equation (1) was used to calculate the expected responses for possible θ_o and φ_o values with the known $B_l(t)$ and $B_t(t)$. The magnetic field, m(t), was calculated for all possible combinations of θ_o and φ_o in one degree increments between 0 and 90 degrees. Then the orientation of the pipe was determined by finding the θ_o and φ_o that minimized the squared differences between the calculated and measured responses. Data was collected with the pipe rotated in the XY plane and the XZ plane (in 15 degree increments). The following figures illustrate the error surfaces for two pipe orientations and the calculated θ_o and φ_o. The results show that measuring responses while transmitting on X-only, Y-only, and Z-only are enough to determine pipe orientation.

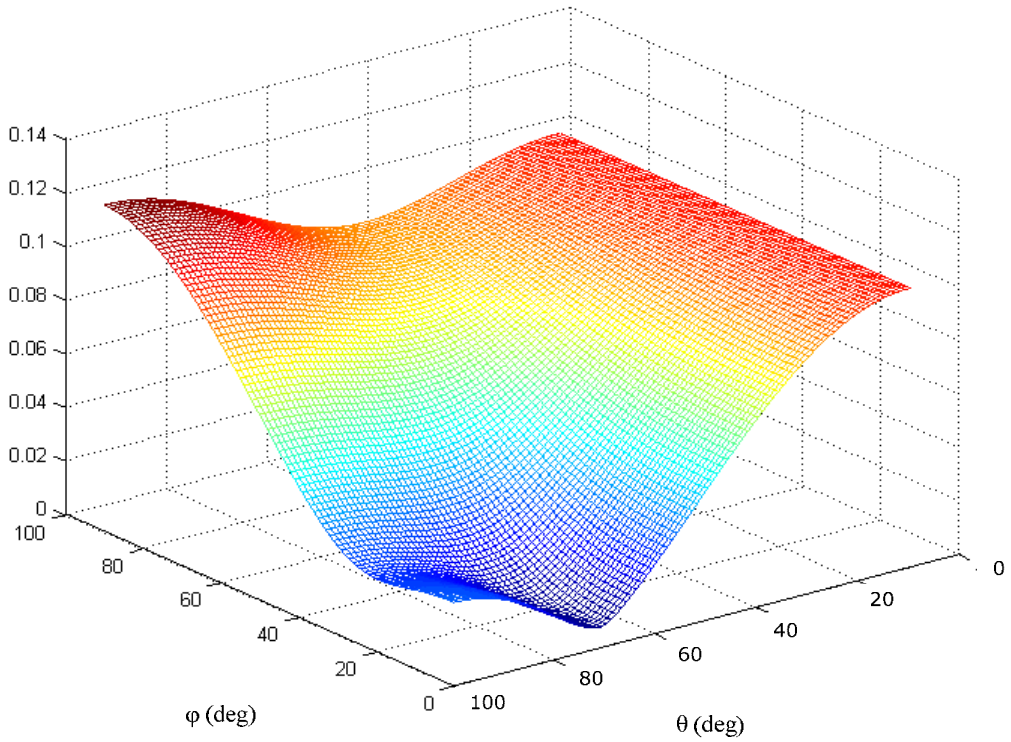

Figure 75 Position: XZ30, Measured Position: φ= 0, θ= 61

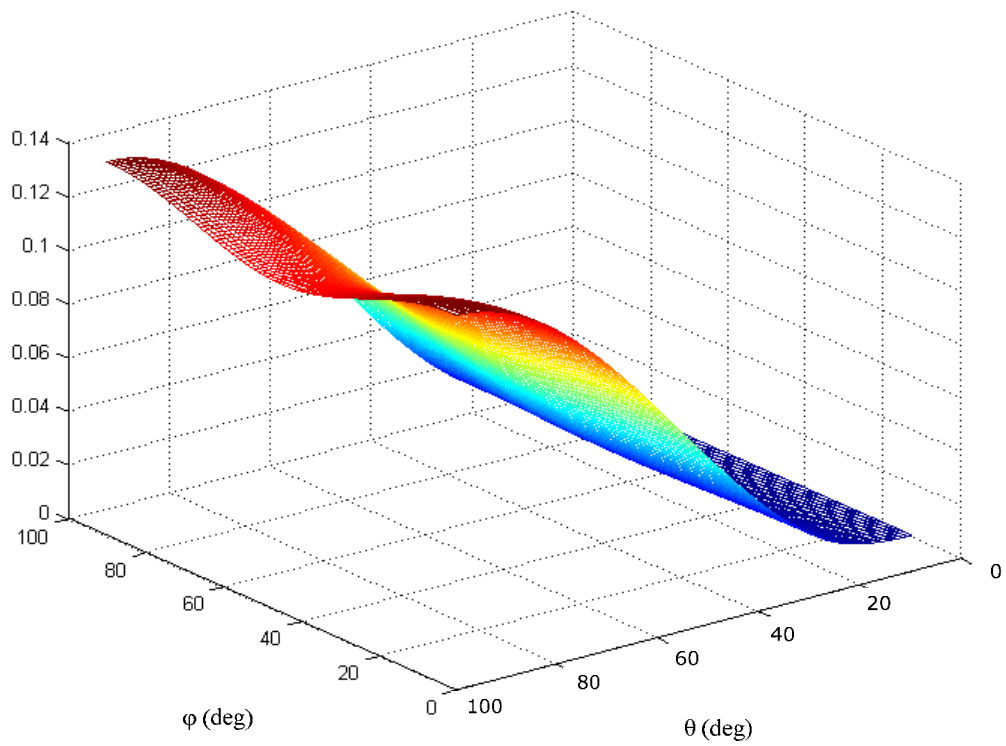

Figure 76 Position: Z0, Measured Position: φ= xx , θ = 0

Table 4 through Table 6 show the mean and standard deviation of the errors between the actual and measured angles for three different object depths. The results show that the orientation of the pipe was determined to be within ±10 degrees of its actual position, with only one exception for the XY75 position. Are we goin to leave this angle as is as well?

Table 4 Actual vs. Measured Pipe Position for d = 12 inches

Target Orientation	Nominal φ	Calculated φ	Nominal θ	Calculated θ
X0	0	5	90	90
XY15	15	13	90	90
XY30	30	27	90	90
XY45	45	41	90	90
XY75	75	59	90	90
Y0	90	80	90	90
XZ15	0	0	75	75
XZ30	0	0	60	61
XZ45	0	0	45	45
XZ60	0	0	30	32
XZ75	0	0	15	12
Z0	xx	xx	0	0

Table 5 Actual vs. Measured Pipe Position for d = 16 inches

Target Orientation	Nominal φ	Calculated φ	Nominal θ	Calculated θ
Y0	90	90	90	81
XY60	60	61	90	90
XY75	75	75	90	90
X0	0	11	90	78
Z0	xx	xx	0	8
YZ15	90	90	75	80
XZ15	0	11	75	73

Table 6 Actual vs. Measured Pipe Position for d = 20 inches

Target Orientation	Nominal φ	Calculated φ	Nominal θ	Calculated θ
Y0	90	90	90	90
XY60	60	64	90	90
XY75	75	73	90	90
X0	0	0	90	76
Z0	xx	xx	0	12
YZ15	90	90	75	73
XZ15	0	9	75	74

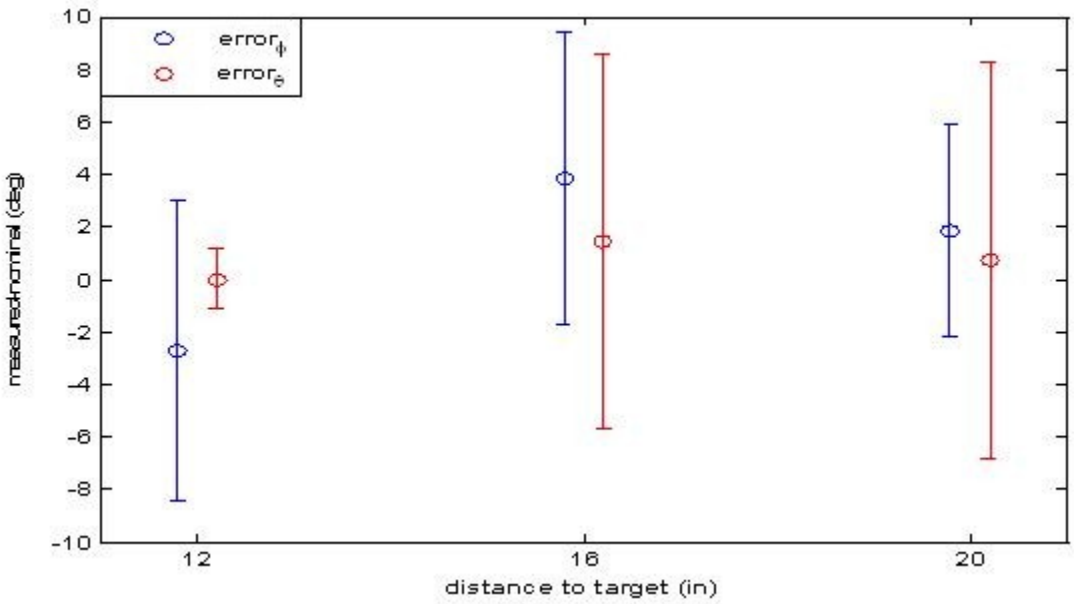

Figure 77 Summary of pipe data for different depths

The data for most of this analysis was collected with the objects centered under the antenna. Some pipe data was also collected with the pipe in off center positions (shifted along the X- or Y-axis) with results shown in Table 7. Except for the Z0-Y offset position, the results appear comparable to those where the pipe was centered and distances greater than 12 inches.

Table 7 Actual vs. Measured Pipe Position for Off Center Positions

Target Orientation	Nominal φ	Calculated φ	Nominal θ	Calculated θ
Z0-Y offset	xx	xx	0	20
Z0-X offset	xx	xx	0	11
X0-Y offset	0	10	90	90
Y0-X offset	90	90	90	90

Conclusions

The first year of the project successfully constructed the basic framework for the 3DSMF sensor system while the second year of the project was primarily devoted to sensor integration and optimization in preparation for data acquisition. A number of unexpected problems arose during the laboratory shakedown testing of this new technology. A side benefit of these problems was that we developed several new technologies that are beneficial to pulse induction metal detection in general. The prototype is a versatile test-bed to explore variations in transmitter characteristics and alternate receiver geometries. Laboratory testing and data analysis during the final year of the project shows that the 3DSMF Sensor System may not only identify targets (using ATR algorithms with a library of UXO time decay constants) but also determine spatial orientation of the targets to facilitate remediation.

The original system concept was that the transmitters would "steer" through a series of angles in an attempt to match the MFV to the body of revolution of an unknown target. The data analysis conducted to date has used responses collected after successive maximum transmissions of X-, Y-, and Z-only MFVs. It is unknown whether better results would be obtained with the steered MFVs or possibly with simultaneous X-, Y-, and Z-transmissions. Each option has an impact on the dwell time of the 3DSMF Sensor System over a target due to the number of transmissions required.

The current year's results, from testing and data analysis of simple targets, show promise of confirming the 3DSMF identification concept when using libraries of target time decay constants. Additional analysis of laboratory data would be possible with the current prototype, however field testing and confirmation on "blind" UXO lanes requires construction of a ruggedized version.

ACKNOWLEDGEMENT

This research has been supported by the Strategic Environmental Research and Development Program (SERDP), under contract number DACA72-02-C-0030.

REFERENCES

1. Examples include: Geonics Limited EM-63 experimental three-axis metal detector; Zonge Engineering experimental three-axis metal detector; Blackhawk Geometrics experimental three-axis metal detector.
2. Nelson, C. V., "Method for metal object identification using a three-dimensional steerable magnetic field antenna," US Patent Application 20040178794.
3. Nelson, C. V., Mendat, D. P., and Huynh, T. B., "Three-dimensional steerable magnetic field antenna for metal target classification," Detection and Remediation Technologies for Mines and Minelike Targets VIII, Proceedings of SPIE Vol. 5089 (2003).
4. Baum, C. E., Detection *and Identification of Visually Obscured Targets*, C. E. Baum, Editor, Taylor & Francis, 1999.
5. Nelson, C. V., Huynh, T. B., Writer, T., and Lacko, P. R., and, "Horizontal electromagnetic field sensor for detection and classification of metal targets," Detection and Remediation Technologies for Mines and Minelike Targets VI ,Proceedings of SPIE, Vol. 4394, pp. 65-74 (2001).
6. Nelson, C. V., Cooperman, C. B., Schneider, W., Wenstrand, D. S., and Smith, D. G., "Wide bandwidth time-domain electromagnetic sensor for metal target classification," *IEEE. Trans. Geoscience and Remote Sensing,* July 2001.
7. Nelson, C. V., and Huynh, T. B., "Wide bandwidth, time decay responses from low-metal mines and ground voids," Detection and Remediation Technologies for Mines and Minelike Targets VII, Proceedings of SPIE Vol. 4742, pp. 55-64, (2002).
8. Nelson, C. V., and Huynh, T. B., "Spatial scanning time-domain electromagnetic sensor: high spatial and time resolution signatures from metal targets and low-metal content land mines," Detection and Remediation Technologies for Mines and Minelike Targets VII, Proceedings of SPIE Vol. 4742, pp. 766-775, (2002).
9. Black, C., McMichael, I., and Nelson, C., "Preliminary investigation of the multi-mode electromagnetic target discriminator," Detection and Remediation Technologies for Mines and Minelike Targets IX, Proceedings of SPIE Vol. 5415, pp. 283-290 (2004)
10. Smythe, W. R., "Static & Dynamic Electricity," McGraw-Hill, 3rd ed., 1968.
11. Nelson, C. V., "Switched coil receiver antenna for metal detector", US Patent Application Pending.

Additional detailed information on 2003 and 2004 project activities (which are not explicitly referenced in this report) may be found in the previous annual project reports:

- "Three-dimensional Steerable Magnetic Field Antenna Sensor System for Metal Target Classification," UX-1314, 2003 Annual Report
- "Three-Dimensional Steerable Magnetic Field (3DSMF) Sensor System for Classification of Buried Metal Targets," SERDP Project UX-1314, Annual Report, STN-04-215, December 2004.